

Banner appropriate to article type will appear here in typeset article

On the effect of adverse pressure gradients on wall-pressure statistics in a controlled-diffusion aerofoil turbulent boundary layer

A. Caiazzo¹†, S. Pargal^{1,2}, H. Wu³, M. Sanjosé⁴, J. Yuan², and S. Moreau¹

¹Department of Mechanical Engineering, University of Sherbrooke, Sherbrooke, J1K2R1, QC, Canada

²Department of Mechanical Engineering, Michigan State University, MI 48824, USA

³Department of Plasma Research, General Fusion, Burnaby, British Columbia, V3N 4T5, Canada

⁴Department of Mechanical Engineering, École de Technologie Supérieure, Montréal, H3C1K3, QC, Canada

(Received xx; revised xx; accepted xx)

Wall-pressure and velocity statistics in the turbulent boundary layer (TBL) on a cambered controlled-diffusion aerofoil at 8° incidence, a Mach number of 0.25, and a chord-based Reynolds number $Re_c = 1.5 \times 10^5$ are analyzed at four locations on the suction side with zero and adverse pressure gradients (ZPG and APG), characterized by increasing Reynolds numbers based on momentum thickness, $Re_\theta = 319, 390, 877$ and 1036. The strong APG yields a highly non-equilibrium TBL at the trailing edge that significantly affects the turbulent flow statistics. Different normalizations of the full wall-pressure statistics involved in trailing-edge noise are analyzed for the first time in such strong APG with convex curvature, and compared with available experimental and numerical data. Good overall agreement is found in the ZPG region, and most results obtained in previous APG TBL can be extended to the present highly non-equilibrium case. The presence of strong APG augments the intensity of wall-pressure fluctuations noticeably at low frequencies, shortens the streamwise and broadens the spanwise coherence of wall-pressure fluctuations in both time and space, and significantly reduces the convection velocity. The wall-pressure power spectral density are found to scale with the displacement thickness, the Zaragola-Smits velocity and the root-mean-squared pressure, the latter possibly being replaced by the local maximum Reynolds shear stress. The other two key parameters to trailing-edge noise modelling, the spanwise coherence length and the convection velocity, rather scale with displacement thickness and friction velocity respectively.

1. Introduction

The wall-pressure fluctuations induced by a turbulent boundary layer (TBL) constitute an important source of noise and vibration in many applications. Such fluctuations, caused by eddies correlated over limited regions in the boundary layer, result in flow-induced loads that can either radiate noise directly or excite the underlying structure generating vibration and

† Email address for correspondence: caiazzo89anna@gmail.com

36 noise, mainly in the low to mid-audio frequency range, where human annoyance to noise
 37 is particularly important. This topic is also of interest for many engineering problems. A
 38 few examples among many are fatigue cracking on panels of an aircraft fuselage induced
 39 by high-speed turbulent flow, or cabin noise transmitted by flexible structures loaded by
 40 TBLs excitation. In marine transportation, the noise generated by wall-pressure fluctuations
 41 has become quite important when considering the need for improved inboard comfort
 42 in high-speed ships. In particular, acoustic waves created by the scattering of the wall-
 43 pressure fluctuations at a sharp-edged body, such as a wing or a fan blade, are the cause
 44 of broadband noise, also known as trailing-edge (TE) noise (Brooks & Hodgson 1981;
 45 Tam & Yu 1975; Lee *et al.* 2021). As indicated in most aerofoil TE noise models based
 46 on acoustic analogies (Ffowcs-Williams & Hall 1970; Howe 1978; Curle 1955), the wall-
 47 pressure fluctuations can be an efficient sound source of dipole type that can be dominant at
 48 low Mach numbers. Indeed, such a noise mechanism is responsible for part or most of the
 49 airframe, propeller, low and high speed rotor and wind turbine noise, as well as other noise
 50 problems.

51 In order to predict the disturbance produced by such turbulent flows, it is first necessary
 52 to model all the fluctuating properties that characterize the flow field. Indeed, as indicated
 53 in Blake (1986, 1970) and Bull (1996) for instance, the common modeling approach used
 54 to evaluate the structural response to a wall-pressure excitation induced by TBL requires
 55 a proper representation of the underlying structural forcing function, which presumes the
 56 correct representation of single and two-point turbulent wall-pressure statistics i.e. power
 57 spectral densities (PSD) , spatial and wavenumber spectra, convection or phase velocities.
 58 Furthermore, to address TE noise problems, Amiet's model and its extension (Amiet 1976;
 59 Roger & Moreau 2005; Moreau & Roger 2009; Roger & Moreau 2012), which relies on
 60 Curle's analogy combined with a compressible linearized Euler model for the wall-pressure
 61 fluctuations on an infinitely thin flat plate at zero incidence, is one of the most popular
 62 method as it only requires the prescription of PSD spectra near the TE, as well as the spatial
 63 cross-spectrum and convection velocities. **Indeed, the PSD of the far-field acoustic pressure**
 64 **at any observer located at $\mathbf{X} = (X_1, X_2, X_3)$, for any angular frequency ω , generated by a flat**
 65 **plate of chord length c and span L reads:**

$$66 \quad S_{pp}(\mathbf{X}, \omega) \approx \left(\frac{kcX_2}{4\pi S_0^2} \right)^2 \frac{L}{2} \left| I \left(\frac{\omega}{U_c}, k \frac{X_3}{S_0} \right) \right| \phi_{pp}(\omega) L_z \left(\omega, k \frac{X_3}{S_0} \right), \quad (1.1)$$

67 where k is the acoustic wave number, S_0 the corrected distance to the observer, I the
 68 analytical radiation integral (or acoustic transfer function) given in Roger & Moreau (2005),
 69 U_c the streamwise convection velocity, ϕ_{pp} the wall-pressure spectrum and L_z the spanwise
 70 coherence length. It is then clear that a comprehensive study on scaling laws should consider
 71 all three parameters.

72 In such a context, TBL characterization, both in measurements, simulations and modeling,
 73 has received a considerable amount of attention. Several experimental measurements have
 74 been carried out over the years on TBL wall-pressure fluctuations in order to estimate
 75 the statistical properties of the flow, mostly in zero pressure gradient (ZPG) TBLs on flat
 76 plates or inside tubes (Willmarth 1956; Bull 1967; Blake 1970; Farabee & Casarella 1991;
 77 Corcos 1962; Arguillat *et al.* 2010). Among them, Arguillat *et al.* (2010) performed direct
 78 measurements of the wavenumber-frequency spectrum of wall-pressure fluctuations beneath
 79 a turbulent plane channel flow in an anechoic wind tunnel, using a rotative array of 63 remote
 80 microphone probes; they analyzed the acoustic and the aerodynamic contributions from
 81 wall-pressure fluctuations by transforming space-frequency data into wavenumber-frequency
 82 spectra, underlining the importance of considering both contributions for an accurate noise

83 prediction. Recently, Van Blitterswyk & Rocha (2017) has published a more complete
84 analysis of the physical relationship between wall-pressure and turbulence, combining a
85 high-resolution wall-mounted microphone array and single hot wires to simultaneously
86 measure both wall-pressure and velocity fluctuations induced by low Reynolds number
87 ZPG TBLs. By performing simple statistical analysis and using a wavelet transform,
88 Van Blitterswyk & Rocha (2017) was able to estimate the contributions from the buffer,
89 logarithmic and outer layers to wall-pressure fluctuations, showing the effect of the hairpin
90 structures contributing to the large-scale motions with increasing Reynolds numbers based
91 on momentum thickness. Fewer authors have focused in depth on adverse pressure gradient
92 (APG) TBL measurements (Bradshaw 1967; Schloemer 1967; Simpson *et al.* 1987; Salze
93 *et al.* 2014, 2015). Among these, Schloemer (1967) has studied the effects of different
94 pressure gradients, such as ZPG, mild APG and favourable pressure gradient (FPG), in
95 a low-turbulence subsonic wind tunnel, comparing his findings for the ZPG case with
96 previous published measurements. Schloemer (1967) drew several conclusions, such as a
97 lower convection velocity ratio in the APG case with respect to ZPG one, a more rapid
98 loss of coherence in the streamwise direction for the APG rather than for ZPG, as well
99 as an increase of the dimensionless spectral density in the low-frequency content due to
100 APG. Later, Salze *et al.* (2014, 2015) used a setup similar to Arguillat *et al.* (2010) to
101 analyze wall-pressure fluctuations with both ZPG and APG TBLs. In the case of Salze
102 *et al.* (2014, 2015), the mean pressure gradient was achieved by inclining the ceiling of the
103 test section, the wall-pressure fluctuations were measured by using a pinhole microphone
104 together with a high-frequency-calibration procedure and the wavenumber-frequency spectra
105 were obtained using a rotating linear antenna of remote microphones. As discussed in the
106 experimental review of Willmarth (1975) and Eckelmann (1988), accurate measurements
107 are difficult due to the pressure transducer size or the wide range of pressure fluctuations or
108 the probes sensitivity. Still today, a complete characterization of TBL wall-pressure spectral
109 data is lacking, and no consistent experimental measurements are available in literature.
110 From a modelling point of view, Bull (1996), Graham (1996), Graham (1997), Caiazzo *et al.*
111 (2016), Caiazzo *et al.* (2018) and others have shown that a stochastic source reconstruction
112 is considered as a good alternative to computational fluid dynamic (CFD) simulations to account
113 for TBL excitations in an early design stage. On the other hand, detailed CFD simulations,
114 i.e. large eddy simulations (LES) or DNS, guide engineering in modelling such turbulent
115 statistics very precisely, addressing most of the complicated non-linear phenomena (Ciappi
116 *et al.* 2019). Kim (1989) has computed DNS of ZPG turbulent channel flow. Later Choi &
117 Moin (1990) revisited this work, computing three-dimensional (3D) wavenumber-frequency
118 spectrum of the wall-pressure fluctuations and defined scaling laws for PSD and convection
119 velocities. They have shown that an appropriate scaling for the different spectra is with outer
120 variables at low frequencies and with inner variables at high frequencies; they observed that
121 a discrepancy can be found between convection velocities as a function of wavenumber and
122 as function of frequency and that the hypothesis of a constant convection velocity is valid
123 only for large-scale structures, corresponding to low frequencies and low wavenumbers. A
124 standard reference case for ZPG TBL flows is the work of Spalart (1988), who has analyzed
125 flows at three Reynolds numbers based on momentum thickness θ ($Re_\theta \equiv U_e \theta / \nu = 300, 670$
126 and 1410, with U_e the TBL edge velocity and ν the kinematic viscosity). Na & Moin
127 (1998) performed DNS of two TBLs, attached and separated, over a flat plate with different
128 pressure gradients, observing that one of the major effects of a pressure gradient is to distort
129 the turbulent velocity profiles. Their results reproduce the experiments of Watmuff (1989).
130 More numerical work on TBL wall-pressure fluctuations on flat plate under APG has been
131 carried out by Abe *et al.* (2005) and Abe (2017), who have investigated the Reynolds-
132 number dependence of the pressure fluctuations. Over the past years, several researchers

133 have discussed the effect of ZPG and APG (Lee & Sung 2008; Schlatter *et al.* 2009a,b;
134 Schlatter & Örlü 2010; Kitsios *et al.* 2016; Monty *et al.* 2011; Vila *et al.* 2017; Bobke *et al.*
135 2017; Volino 2020). In general, due to the limitation found in experimental measurements,
136 DNS have become increasingly used to understand the physics of turbulence and to test
137 scaling laws. Recently, Cohen & Gloerfelt (2018) have studied the influence of the pressure
138 gradients on wall-pressure beneath a TBL by carrying out LES for TBL under FPG, ZPG and
139 both strong and weak APG, denoted as "APGs" and "APGw" respectively; they used inclined
140 plates with different slopes to set the pressure gradients and compared their findings with
141 various data available. However, all the above studies involve equilibrium turbulent boundary
142 layers. As recalled by Cohen & Gloerfelt (2018), this mainly involves three main conditions:

- 143 (i) a power-law relationship between the TBL edge velocity U_e and the curvilinear abscissa
144 s along the wall;
- 145 (ii) a linear variation of the outer length scale with s ;
- 146 (iii) some mean gradient parameters remaining constant along s .

147 Moreover, only a few studies on curved surfaces, i.e. on aerofoils, can be found in which
148 turbulence statistics are studied more in depth (Vinuesa *et al.* 2017; Tanarro *et al.* 2020).
149 Furthermore, most of low- and high-speed **compressing** turbomachinery applications involve
150 cambered, highly loaded aerofoils often operating in strong APG on the verge of separation,
151 characterized by strong variations of Clauser parameter (β_c) and acceleration parameter (K)
152 and consequently strongly non-equilibrium turbulent boundary layers not studied before.

153 The present study thus focuses on both ZPG and varying APG effects in strongly non-
154 equilibrium TBLs, by comparing turbulent statistics (both wall-pressure and velocity fields)
155 developed over the **same** curved suction side of a cambered Controlled Diffusion (CD)
156 aerofoil. A three-dimensional compressible Navier-Stokes direct numerical simulation (NS-
157 DNS), described in Wu *et al.* (2018), of the flow over a CD aerofoil at a 8° geometrical
158 angle of attack, is used. The considered chord-based Reynolds number is $Re_c = 1.5 \times 10^5$
159 and the free-stream Mach number is $M = 0.25$. The purpose of this study is to enrich the
160 lack of DNS data in ZPG and APG TBLs on aerofoils by investigating in detail turbulent
161 statistics at four increasing Reynolds numbers based on the momentum thickness. Such a
162 CD profile, used in several previous studies by Roger & Moreau (2005), Wang *et al.* (2009),
163 Wu *et al.* (2018), Wu *et al.* (2019) and others, **belongs to a family of thin aerofoils with**
164 **small relative thickness and mild camber typical of compressing machines. Indeed, it is also**
165 representative of many modern industrial applications i.e. turboengine compressor and fan
166 blades, automotive engine cooling fan, and aerospace heat and ventilation air-conditioning
167 systems. It employs specific characteristics to carefully control flow and aerodynamic losses
168 around the aerofoil surface by controlling the growth of the boundary layer (i.e. its diffusion).
169 The CD aerofoil has been extensively studied both experimentally and numerically, and
170 represents a solid database for studies on both aerodynamics and aeroacoustics (Moreau
171 2016). This aerofoil is characterized by a chord length $c = 0.1356$ m, a 4% thickness to chord
172 ratio and a camber angle of 12° . The numerical case considered here has been developed in
173 order to reproduce the experimental set-up performed in the anechoic open jet wind-tunnel
174 of the Université de Sherbrooke (UdeS) (Padois *et al.* 2015; Jaiswal 2020), in which remote
175 microphone probes are distributed over the pressure and suction sides of the CD aerofoil
176 to measure wall-pressure fluctuations. The boundary layer developing over the suction side
177 of the CD aerofoil first encounters a laminar separation bubble (LSB) at the leading edge
178 (LE) that triggers the transition to turbulence. The TBL then encounters a FPG, followed by
179 a ZPG around mid-chord, and finally, an APG growing fast till the TE due to the aerofoil
180 camber. The same sensor locations on the CD aerofoil as in the experimental set-up have
181 been considered for statistical analyses in the compressible NS-DNS (Wu *et al.* 2018). In
182 particular, data from four sensors on the suction side of the aerofoil are studied here. Those

183 are representative of TBLs with ZPG or APG. Note that the short FPG region is not directly
 184 considered here, but its effect on the ZPG statistics is also assessed.

185 The paper is organized as follows. Firstly, in Section 2, the details of the numerical set-up
 186 are recalled, together with a summary of the signal processing methods adopted. In Section 3,
 187 the TBL characteristics and velocity statistics are presented. A discussion of the higher order
 188 statistics results is given in Section 4, compared with wall-pressure measurements taken in
 189 the anechoic wind tunnel at UdeS and with previous published DNS data obtained in similar
 190 conditions. In particular, the dependence of the convection velocity ratios on wavenumbers,
 191 frequency and spatial separations is discussed in detail for the ZPG and APG parts of the
 192 aerofoil boundary layer. Finally, some conclusions are drawn for this highly non-equilibrium
 193 TBL with curvature effect.

194 2. Numerical case

195 This section will briefly recall the numerical set-up used to generate the database analyzed
 196 in the present study. It corresponds to a 3D compressible NS-DNS performed by Wu
 197 *et al.* (2019) of the airflow over the CD aerofoil embedded in the potential core of
 198 the jet of the anechoic wind tunnel at UdeS as discussed in Padois *et al.* (2015). A
 199 computational [six-block H-O-H structured](#) mesh of $3341 \times 279 \times 194$ grid points is used
 200 in the streamwise (x), wall-normal (y) and spanwise (z) directions respectively. The total
 201 grid size is 345×10^6 nodes. The compressible Navier-Stokes equations are solved with
 202 the multi-block structured code HiPSTAR (High Performance Solver for Turbulence and
 203 Aeroacoustics Research) (Sandberg 2015). The spatial discretization involves both a five-
 204 point fourth-order central standard-difference scheme with Carpenter boundary stencils in
 205 the streamwise and crosswise directions (Carpenter *et al.* 1999), and a spectral method
 206 using the FFTW3 library in the spanwise direction. The time discretization is achieved
 207 by an ultra-low-storage five-step fourth-order Runge–Kutta scheme (Kennedy *et al.* 1999).
 208 Characteristic-based boundary conditions are also used to prevent spurious reflections at
 209 the computational domain boundaries (Sandberg & Sandham 2006; Jones *et al.* 2008). A
 210 complete analysis of the numerical set-up that allowed the analysis of both aerodynamics
 211 and acoustics is documented in Wu *et al.* (2019, 2020).

212 The volume data around the aerofoil are recorded at a sampling frequency of 78 kHz for
 213 7 flow-through times, $T = c/U_\infty$, with free-stream velocity $U_\infty = 16 \text{ m s}^{-1}$. A constant
 214 dimensionless time step of $\Delta t = 7.5 \times 10^{-6}$ is used. The space-time database is extracted at
 215 different locations on the aerofoil assuming a spanwise extent of 12% chord; this length is
 216 determined to be sufficient to get fully decorrelated turbulence in the span (Wu *et al.* 2019;
 217 Moreau & Roger 2005; Wang *et al.* 2009). The locations of the experimental wall-pressure
 218 probes considered over the suction side of the CD aerofoil are along the streamwise direction
 219 as shown in figure 1. Sensors 7 and 9 are approximately located at mid chord and sensors 21
 220 and 24 near the TE.

221 The mean pressure distribution over the surface of the CD aerofoil is analyzed in figure 2
 222 through the mean wall-pressure coefficient distribution,

$$223 \quad -C_p = -\frac{\bar{p} - p_\infty}{\frac{1}{2}\rho U_\infty^2}, \quad (2.1)$$

224 where p_∞ and ρ are the reference static pressure and air density taken at the inlet respectively.
 225 The mean wall-pressure coefficient calculated from the DNS is also compared with wall-
 226 pressure measurements by Jaiswal *et al.* (2020) and Jaiswal (2020), [taken at several locations](#)
 227 [over the suction and pressure side of the CD aerofoil](#). As seen in figure 2, a small plateau
 228 between $x/c = -1$ and $x/c = -0.9$ indicates a small laminar recirculation bubble at the

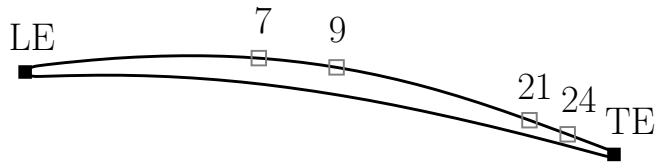


Figure 1: Remote microphone probes locations on the CD aerofoil. Numbers show sensor indices designated in Wu *et al.* (2019).

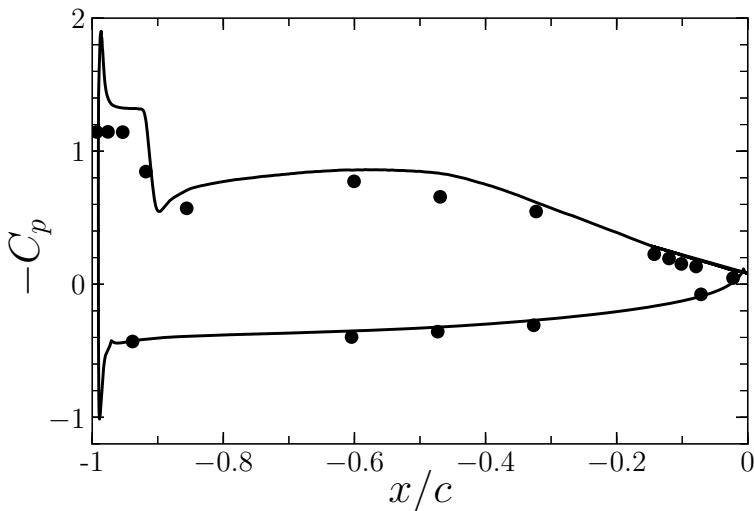


Figure 2: Pressure coefficient distribution, C_p , on the CD aerofoil: —, DNS (Wu *et al.* 2019); •, experiment (Jaiswal *et al.* 2020; Jaiswal 2020).

229 aerofoil LE that triggers the transition to turbulence in the bubble shear layer and consequently
 230 an attached turbulent flow. After the reattachment point, the pressure gradient increases along
 231 the CD aerofoil. The flow is first subjected to a FPG, then to a ZPG around mid-chord and
 232 finally to an APG downstream due to the aerofoil camber. On the pressure side, the flow
 233 is laminar and attached until the TE where it transitions to turbulence with a small vortex
 234 shedding appearing in the near wake, mixing with the turbulent flow on the suction side (Wu
 235 *et al.* 2018; Moreau *et al.* 2011; Neal 2010). By comparison with the set of experimental
 236 data produced at UdeS (Jaiswal *et al.* 2020; Jaiswal 2020), the DNS distribution gives a good
 237 prediction of the pressure coefficient on the aerofoil, except for a slightly higher pressure
 238 plateau within the thin laminar separation bubble at the LE (Wu *et al.* 2020), see figure 2.

239 As shown in figure 1, the four points of the aerofoil suction side analyzed correspond to
 240 ZPG (sensors 7 at $x/c = -0.60$ and 9 at $x/c = -0.47$) and APG (sensors 21 at $x/c = -0.14$
 241 and 24 at $x/c = -0.08$) locations. For each location a volume of data containing the pressure
 242 and velocity distributions is extracted.

2.1. Signal processing

243

244 A summary of the signal processing adopted throughout the paper is presented here. The
 245 DNS volume data are appropriately scaled to obtain dimensional quantities. In particular, the
 246 numerical pressure data are rescaled by ρU_∞^2 . The wall-pressure statistics are then computed
 247 for the four locations corresponding to sensors 7, 9, 21 and 24.

248

249 For all four sensor locations and even for those close to the TE in the strong APG region, the
 250 local pressure field has been found homogeneous in planes parallel to the wall and stationary
 251 in time, both numerically (Grasso *et al.* 2019) and experimentally (Jaiswal *et al.* 2020;
 252 Jaiswal 2020). In practical applications, only single time histories of the stochastic variable
 253 are available, and thus the stationary process is normally assumed to be ergodic. Under
 254 such conditions, the space-time cross-correlation function of the wall-pressure fluctuations
 $p' = p - \bar{p}$ at two arbitrary space-time points is defined as

255

$$R_{pp}(\boldsymbol{\xi}; \tau) = \lim_{T \rightarrow \infty} \frac{1}{T} \int_0^T p'(\mathbf{x}, t) p'(\mathbf{x} + \boldsymbol{\xi}, t + \tau) dt, \quad (2.2)$$

256

257 where $\boldsymbol{\xi}$ is the spatial separation vector between two points located at \mathbf{x} and $\mathbf{x} + \boldsymbol{\xi}$ with time
 258 delay τ . In this way, the random sample in space and time is compressed into a much shorter
 259 function of $\boldsymbol{\xi}$ and τ . The cross-spectral density (CSD) is then calculated with a simple fast
 260 Fourier transformation using a Welch periodogram technique and Hanning windowing with
 zero padding (Salze *et al.* 2014),

261

$$\Psi_{pp}(\boldsymbol{\xi}; \omega) = \frac{1}{2\pi} \int_{-\infty}^{\infty} R_{pp}(\boldsymbol{\xi}, \tau) \exp(-i\omega\tau) d\tau. \quad (2.3)$$

262

263 The spectra are computed using a Welch periodogram method with 16 windows, each
 264 containing 512 points, and with 50% overlap. The high frequency numerical noise is filtered
 265 out using a Butterworth filter. By doing a two-dimensional (2D) spatial Fourier transform
 266 of $\Psi_{pp}(\boldsymbol{\xi}; \omega)$ with the cross-correlation spectra for each time block averaged together, the
 267 CSD function in the wavenumber-frequency domain is then computed by discretizing the
 following Fourier integral

268

$$\Psi_{pp}(\mathbf{k}; \omega) = \frac{1}{(2\pi)^2} \int \int_{-\infty}^{\infty} \Psi_{pp}(\boldsymbol{\xi}; \omega) \exp(-i\mathbf{k}\boldsymbol{\xi}) d\boldsymbol{\xi}, \quad (2.4)$$

269

270 where $\mathbf{k} = (k_x, k_z)$ is the two-dimensional wavevector (Bull 1996), with k_x and k_z the
 271 streamwise and spanwise wavenumbers respectively. The PSD or single-point wall-pressure
 272 spectrum (i.e. auto-spectrum), ϕ_{pp} , at a given angular frequency ω , is related to the space-
 time correlation function and the wavenumber-frequency spectrum by:

273

274

$$\begin{aligned} \phi_{pp}(\omega) &= \frac{1}{2\pi} \int_{-\infty}^{\infty} R_{pp}(0; \tau) \exp(-i\omega\tau) d\tau, \\ &= \int \int_{-\infty}^{\infty} \Psi_{pp}(\mathbf{k}; \omega) d\mathbf{k}. \end{aligned} \quad (2.5)$$

275

276 The resolved normalized frequency range is $0 \leq \omega \delta^* / U_\infty \leq 5.53$ (where δ^* is the boundary
 277 layer displacement thickness) with a frequency resolution of $\Delta\omega = 1.4 \times 10^{-3} U_\infty / \delta^*$ and a
 278 wavenumber resolution of $\Delta k_x = 0.12 / \delta^*$ in the streamwise direction, and $\Delta k_z = 0.14 / \delta^*$ in
 the spanwise direction.

Case	x/c	Re_θ	Re_τ	β_c	K	$H = \delta^*/\theta$ $\times 10^6$
Sensor 7, ZPG	-0.60	319	178	0.005	-0.09	1.61
Sensor 9, ZPG	-0.47	390	185	0.28	-0.97	1.61
Sensor 21, APG	-0.14	877	210	4.82	-3.85	1.86
Sensor 24, APG	-0.08	1036	203	8.31	-2.66	2.00
Choi & Moin (1990), ZPG	-	287	180	-	-	1.62
Cohen & Gloerfelt (2018), ZPG	-	1693	608	0	0	1.46
Cohen & Gloerfelt (2018), APGw	-	2462	692	0.44	-0.16	1.53
Cohen & Gloerfelt (2018), APGs	-	3125	688	1.41	-0.3	1.63
Na & Moin (1998), ZPG	0.50/c	586	329	-0.35	0.93	1.41
Na & Moin (1998), APG	0.85/c	1229	424	1.78	-1.4	1.54
Spalart (1988), ZPG	-	300	150	-	-	1.66
Tanarro <i>et al.</i> (2020), APG (NACA4412)	0.75	1666	366	3.59	-	1.74
Hu (2021), ZPG	-	4889	1439	0.1	-	1.41
Hu (2021), APG	-	8670	1388	6.0	-	1.75
Schloemer (1967), ZPG	-	4500	1603	-	-	1.34
Schloemer (1967), APG	-	7380	1710	3.34	-	1.58

Table 1: Properties of the TBL for the current DNS data and for several existing studies in the literature.

279 3. Boundary layer development

280 The TBL characteristics calculated from the DNS data on the aerofoil suction side of figure
281 1 are shown and discussed here. These distributions are compared with results of several
282 available numerical and experimental datasets (Schloemer 1967; Brooks & Hodgson 1981;
283 Spalart 1988; Watmuff 1989; Na & Moin 1998; Schlatter *et al.* 2009a,b; Vinuesa *et al.* 2017;
284 Cohen & Gloerfelt 2018; Tanarro *et al.* 2020; Hu 2021).

285 In table 1, the properties of the TBL for the current DNS at the four sensors locations are
286 summarized. The flow properties for DNS cases of Choi & Moin (1990), Spalart (1988),
287 Tanarro *et al.* (2020), and Na & Moin (1998) (including both ZPG TBL, $x = 0.50$, attached
288 APG TBL, $x = 0.85$, and separated APG TBL at $x/\delta_{in}^* = 120$) are also reported in table 1.
289 Additionally, the ZPG, APGs and APGw cases of Cohen & Gloerfelt (2018) are also included
290 in table 1. These data are also considered later for comparison of PSD and the convection
291 velocities.

292 Here, $Re_\tau = u_\tau \delta / \nu \equiv \delta^+$ is the friction Reynolds number or Kármán number, with
293 $u_\tau = \sqrt{\tau_w / \rho}$ the friction velocity, $\tau_w = \mu \frac{\partial U}{\partial y}|_{y=0}$ the wall shear stress (U is the streamwise
294 mean velocity component and y is the wall-normal distance from the wall) and δ the boundary
295 layer thickness. The latter is calculated based on the conservation of the stagnation pressure
296 $p_t = \rho u_t^2 / 2 + p_\infty$ outside the boundary layer for the present low speed flow; u_t^2 is the velocity
297 magnitude squared. The edge of the boundary layer is considered reached when p_t is 95%
298 of its maximum value in the wall-normal direction (Sanjosé & Moreau 2018; Griffin *et al.*
299 2021). This criterion was also used in the boundary-layer data extraction by Christophe *et al.*
300 (2015); the criterion is necessary as the edge velocity is not constant around the aerofoil in the
301 jet potential core. $\beta_c = \delta^* / \tau_w (dp/ds)$ is the Clauser parameter, with dp/ds the streamwise
302 mean pressure gradient on the wall. $K = \nu / U_e^2 (dU_e/ds)$ is the acceleration parameter.
303 $H = \delta^* / \theta$ is the shape factor. β_c and K both vary strongly along the curvilinear abscissa
304 s , which confirms a strongly non-equilibrium turbulent boundary layer on the CD aerofoil
305 suction side according to the above criterion (iii). To quantify this non-equilibrium state, in
306 figure 3, the evolution of β_c as a function of the defect shape factor $G \equiv [(H - 1)/H] u_\tau / U_e$

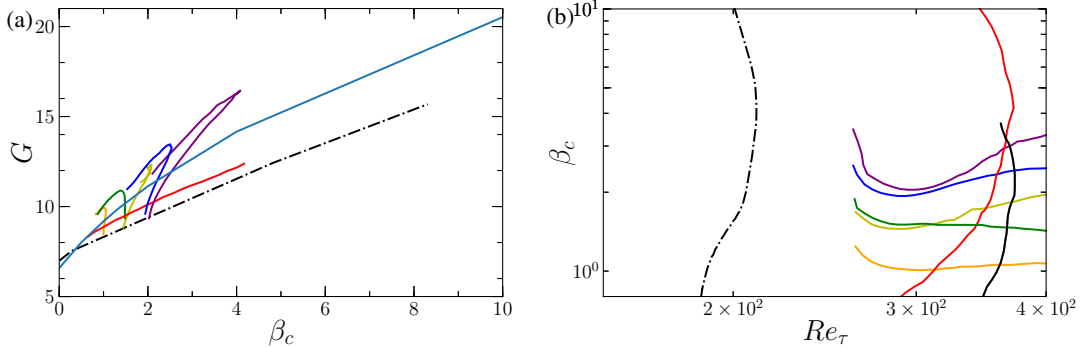


Figure 3: Clauser pressure-gradient parameter β_c as function of (a) defect shape factor G and (b) friction Reynolds number Re_τ . - · - ·, present CD aerofoil DNS; - (light blue) theoretical equilibrium data (Mellor & Gibson 1966); - (green) flat plate DNS for constant and non-constant β_c -cases (Bobke *et al.* 2017): (green) $m = -0.13$ with $\beta_c = [0.86; 1.49]$, (blue) $m = -0.16$ with $\beta_c = [1.55; 2.55]$, (purple) $m = -0.18$ with $\beta_c = [2.15; 4.07]$, (orange) $\beta_c = 1$ and (olive) $\beta_c = 2$; - (red) NACA4412 and (black) NACA0012 aerofoil DNS (Tanarro *et al.* 2020).

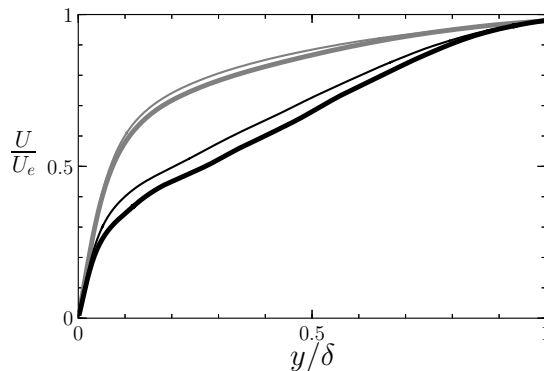


Figure 4: Dimensionless velocity profiles: ZPG locations $x/c = -0.60$ (thin gray line) and $x/c = -0.47$ (thick gray line); APG locations $x/c = -0.14$ (thin black line), $x/c = -0.08$ (thick black line).

307 or the friction Reynolds number Re_τ is shown for the current case and compared with the
 308 theoretical equilibrium turbulent boundary-layer data of Mellor & Gibson (1966), the quasi-
 309 equilibrium cases corresponding to constant and varying β_c simulated by Bobke *et al.* (2017)
 310 (m in caption is the power-law exponent of varying streamwise velocity at the top boundary
 311 to yield near-equilibrium APG flow conditions, based on definition by Townsend (1961)),
 312 and the non-equilibrium flow data from NACA0012 and NACA4412 aerofoils (Tanarro *et al.*
 313 2020). The present simulation is noticeably further away from the theoretical equilibrium
 314 G -factor and presents a faster growth of β_c , yielding a turbulent boundary layer on the verge
 315 of separation for Kármán numbers typical of highly loaded low-speed fans.

316 The normalized velocity profiles for the current DNS case are presented in figure 4. The
 317 profiles obtained at mid-chord locations are similar. Near the TE, a thicker boundary layer
 318 with a lower wall shear stress τ_w is observed, due to APG.

319 In figure 5, the skin-friction coefficient, $C_f = \tau_w / (0.5\rho U_e^2)$, and the shape factor, H , are
 320 plotted against Reynolds number based on momentum thickness. The skin-friction coefficient

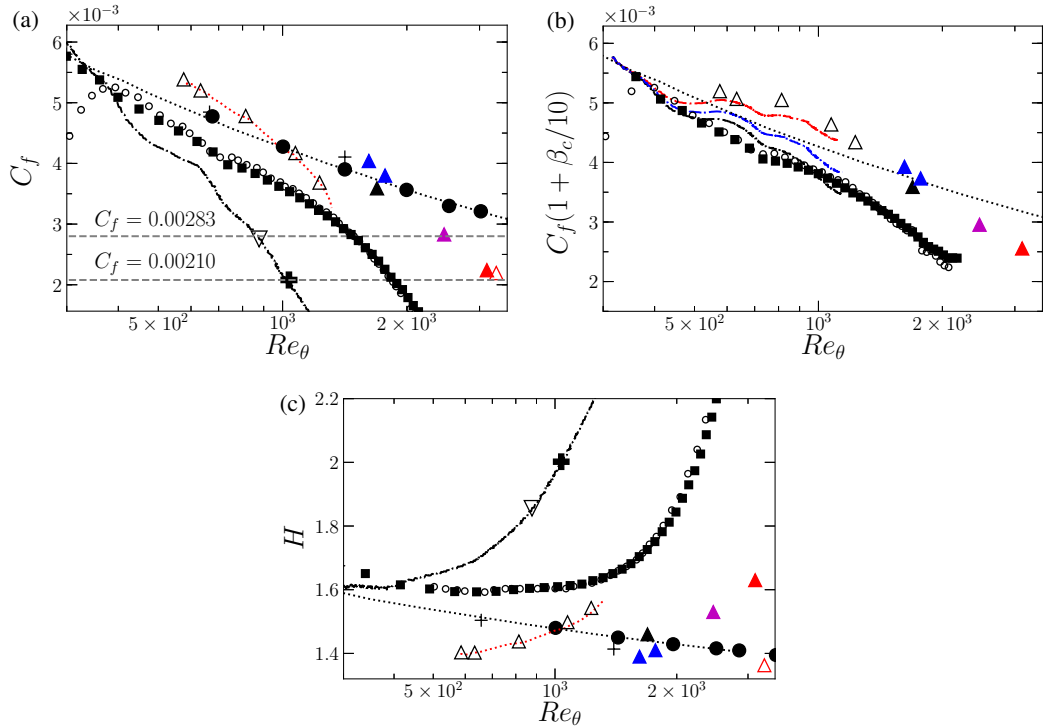


Figure 5: (a) Skin friction coefficient, C_f , (b) corrected with $(1 + \beta_c/10)$, and (c) shape factor, H , versus momentum thickness based Reynolds number: $-\cdot-$, DNS data on the surface of the CD aerofoil, $-\cdot-$ (blue) $C_f(1 + 0.12\beta_c)$, $-\cdot-$ (red) $C_f(1 + 0.15\beta_c)$, APG locations ∇ , $x/c = -0.14$ and $+$, $x/c = -0.08$; $\cdot\cdot\cdot$, empirical correlation by Smits *et al.* (1983) for C_f and correlation form by Monkewitz *et al.* (2007) for H ; \circ , NACA4412 data by Vinuesa *et al.* (2017); \blacksquare , NACA4412 data by Tanarro *et al.* (2020); $+$, data by Spalart (1988); and \bullet , data by Schlatter *et al.* (2009a,b); \blacktriangle , FPG (blue), ZPG (black), APGs (red), APGw (magenta) data by Cohen & Gloerfelt (2018); $\cdot\cdot\cdot$ (red) attached TBL distribution by Na & Moin (1998); and, \triangle , data ($x = 0.5$ m to $x = 0.85$ m) for attached TBL (black) and separated TBL (red) ($x/\delta_{in}^* = 120$) by Na & Moin (1998).

321 decreases with higher Re_θ as the boundary layer develops. Also shown are the empirical
 322 correlation based on the $1/7$ -power law of the form $C_f = 0.024Re_\theta^{1/4}$ by Smits *et al.* (1983),
 323 aerofoil data by Vinuesa *et al.* (2017) and Tanarro *et al.* (2020), and additional reference data
 324 (Spalart 1988; Schlatter *et al.* 2009a,b; Cohen & Gloerfelt 2018; Na & Moin 1998). In the
 325 ZPG zone around $Re_\theta = 320$, the skin-friction coefficient and the shape factor matches well
 326 with the correlation values (Monkewitz *et al.* 2007; Schlatter & Örlü 2010). At higher Re_θ ,
 327 the trend of C_f and H with Re_θ starts to differ: C_f decreases and H increases much faster
 328 in comparison to ZPG correlations. This is caused by the strong APG effects of this highly
 329 non-equilibrium flow as the TE is approached. Such a variation is qualitatively inline with
 330 previous notable studies on aerofoils (Vinuesa *et al.* 2017; Tanarro *et al.* 2020), but with a
 331 stronger APG on the verge of separation, typical of highly loaded low-speed fans. The C_f
 332 corrected with $(1 + \beta_c/10)$ as proposed by Volino (2020) is plotted in figure 5 (b). This
 333 correction with the Clauser pressure gradient parameter improves the C_f correlation, and
 334 collapses all aerofoil data. However, a scatter (though reduced) is still present considering
 335 both airfoil and ZPG data, as shown by the current DNS results with modified Volino (2020)

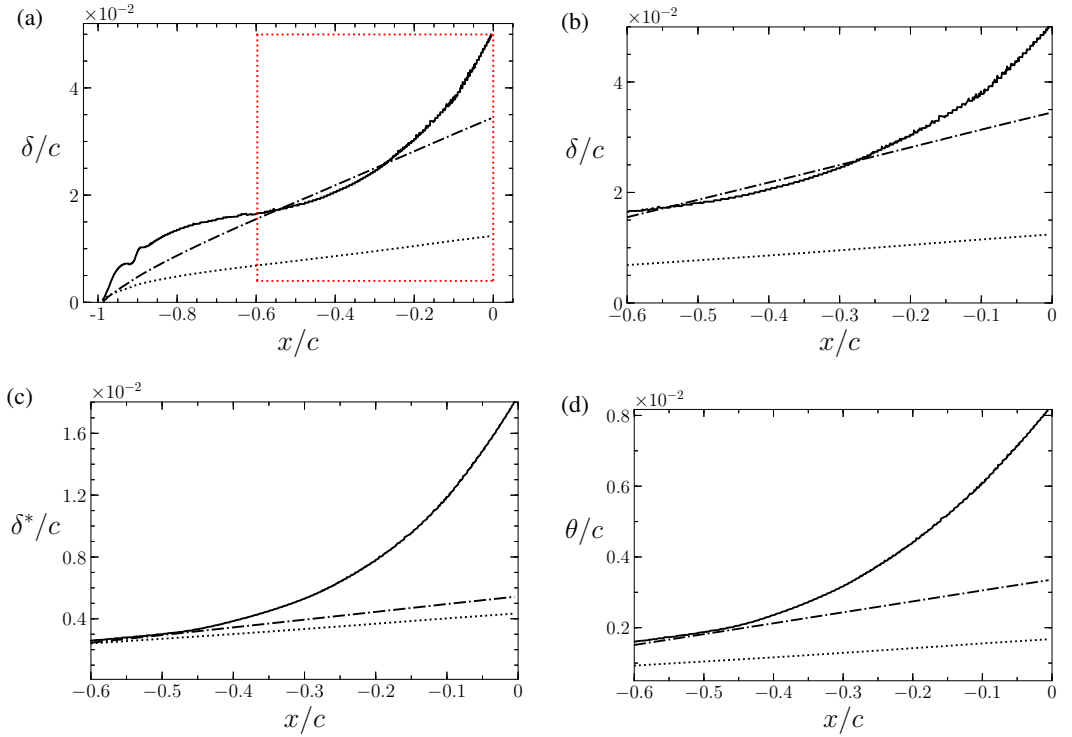


Figure 6: Normalized boundary layer parameters distribution on the surface of the CD aerofoil. (a-b) Boundary layer thickness based on 95% of total pressure; (c) boundary layer displacement thickness and (d) boundary layer momentum thickness; \cdots , laminar flat plate and, $- - -$, turbulent flat plate (Schlichting & Gersten 2017).

336 corrections with different β_c multipliers of 0.12 and 0.15. Therefore, the constant of 0.1 used
 337 by Volino (2020) is not universal and depends on the mean pressure gradient.

338 Figure 6 shows the streamwise variations of δ , δ^* and θ normalized by c , compared to
 339 laminar and turbulent flat plate ZPG boundary layer solutions, obtained assuming fully
 340 laminar or fully turbulent boundary layer from the LE. In figure 6 (a), a hump of δ/c near
 341 the LE is seen as the laminar separation bubble develops; after the hump, the boundary
 342 layer thickness over the CD aerofoil increases after the transition to turbulence, noticeably
 343 so around $x/c = -0.6$ in the ZPG region, where δ/c matches the ZPG turbulent flat plate
 344 boundary layer solution. The red dotted box in figure 6 (a) represents the aerofoil region
 345 considered in figures 6 (b-d), which starts around mid-chord at sensor 7 ($x/c = -0.6$).

346 The boundary layer displacement thickness (figure 6 (c)) and the boundary layer momen-
 347 tum thickness (figure 6 (d)) are obtained by integration of the corresponding velocity profile
 348 across the boundary layer,

$$349 \quad \delta^*(x) = \int_{y=0}^{\delta} \left(1 - \frac{U}{U_e}\right) dy, \quad \theta(x) = \int_{y=0}^{\delta} \frac{U}{U_e} \left(1 - \frac{U}{U_e}\right) dy. \quad (3.1)$$

350 The increasing growth rate of the boundary layer as shown by all three thicknesses is due
 351 to the APG experienced by the boundary layer as it develops in the aft portion of the CD
 352 aerofoil. The departure from ZPG turbulent solutions is consistent with the fact that the TBL
 353 is subjected to strongly non-equilibrium APG.

354 In figure 7, the variations of δ^*/δ_{in}^* and θ/θ_{in} in the APG region are plotted versus the

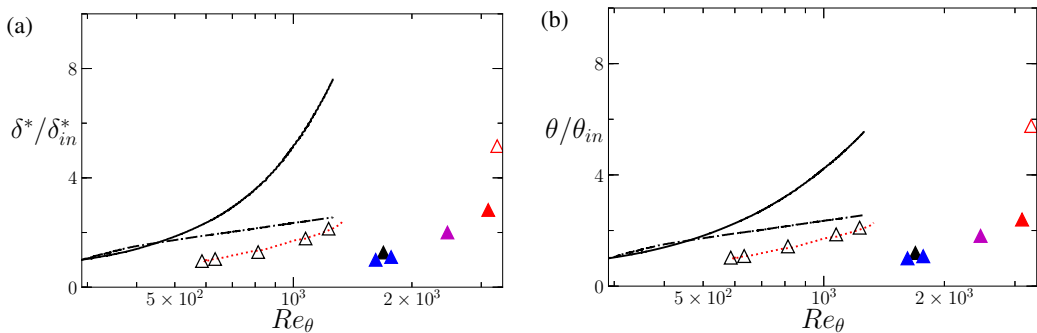


Figure 7: (a) Normalized boundary layer parameters distribution versus momentum thickness based Reynolds number. (a) Boundary layer displacement thickness and (b) boundary layer momentum thickness: —, DNS data on the surface of the CD aerofoil; ▲, ZPG (blue), ZPG (black), APGs (red), APGw (magenta) data by Cohen & Gloerfelt (2018); ··· (red) attached TBL distribution by Na & Moin (1998); and, Δ, data ($x = 0.5$ m to $x = 0.85$ m) for attached TBL (black) and separated TBL (red) ($x/\delta_{in}^* = 120$) by Na & Moin (1998); - - -, turbulent flat plate (Schlichting & Gersten 2017).

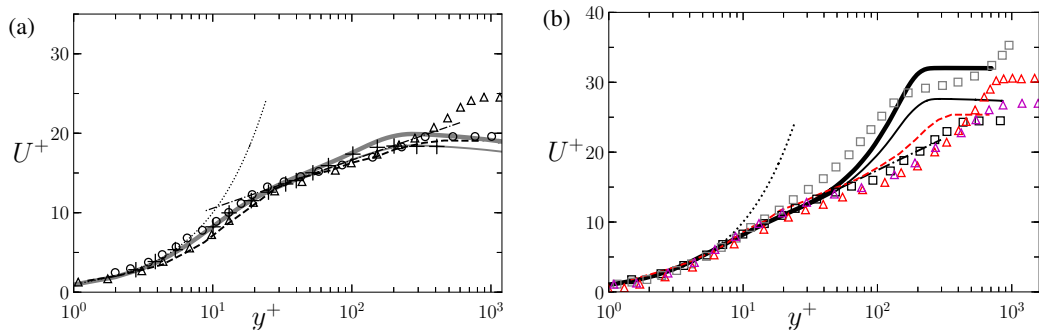


Figure 8: Streamwise velocity profiles as a function of the wall-normal distance scaled on inner variables: (a) ZPG and (b) APG profiles. Present DNS: ZPG locations $x/c = -0.60$ (thin gray line) and $x/c = -0.47$ (thick gray line); APG locations $x/c = -0.14$ (thin black line), $x/c = -0.08$ (thick black line). +, ZPG data by Spalart (1988) with $Re_\theta = 300$; ---, ZPG data $x = 0.5$ m (black) and APG data $x = 0.85$ m (red) data by Watmuff (1989); o, ZPG data $x = 0.5$, □, APG data $x = 0.85$ for attached TBL (black) and separated TBL $x/\delta_{in}^* = 130$ (gray) by Na & Moin (1998); Δ, ZPG (black), APGs (red), APGw (magenta) data by Cohen & Gloerfelt (2018); ···, dimensionless linear law $U^+ = y^+$ and - - -, logarithmic law $U^+ = \frac{1}{\kappa} \ln(y^+) + B$.

355 momentum thickness based Reynolds number, together with the turbulent flat plate solution
 356 (black dotted-dashed line). Such a normalization is consistent with that of Na & Moin (1998)
 357 and Cohen & Gloerfelt (2018) (also shown in figure 7); the subscript ‘in’ indicates quantities
 358 at an upstream ZPG location. For the present DNS, the ‘in’ location is taken at the location
 359 $x/c = -0.6$ (i.e. sensor 7). The present boundary-layer growth on the CD aerofoil is much
 360 faster than in the equilibrium cases of Na & Moin (1998) and Cohen & Gloerfelt (2018),
 361 and only the separated TBL case in Na & Moin (1998) displays similar rapid increase of
 362 boundary layer thicknesses, stressing again the strong non-equilibrium state near the trailing
 363 edge close to flow separation.

364 Streamwise mean velocity profiles scaled on inner variables $U^+ = U/u_\tau$ are plotted versus

365 the normalized wall-normal distance $y^+ = yu_\tau/\nu$ in figure 8. The present DNS results are
 366 compared with the DNS data by Spalart (1988) at $Re_\theta = 300$, Na & Moin (1998) for $x = 0.5$ m
 367 and $x = 0.85$ m, Cohen & Gloerfelt (2018), as well as the experimental data of Watmuff
 368 (1989) for $x = 0.5$ and $x = 0.85$. Figure 8 (a) compares the ZPG data, whereas figure 8 (b)
 369 considers the APG one. The von Kármán constant κ (von Kármán 1931) and the constant B
 370 are prescribed as in Wu *et al.* (2019): $\kappa = 0.41$ and $B = 4.5$ for the ZPG cases, and $\kappa = 0.30$
 371 and $B = -1.38$ for the APG cases. Wu *et al.* (2019) showed that an attached APG flow is
 372 characterized by lower κ values than in a ZPG flow, as well as a negative intercept (B) value,
 373 consistently with what Nickels (2004), Nagib & Chauhan (2008), Monty *et al.* (2011) found
 374 for instance. The present ZPG profiles compare well with the ZPG data of Spalart (1988),
 375 Na & Moin (1998) and Watmuff (1989). Moving towards the TE, a stronger wake region is
 376 seen due to APG effect, as also observed in previous studies (Kitsios *et al.* 2016; Monty *et al.*
 377 2011; Vila *et al.* 2017; Bobke *et al.* 2017; Volino 2020).

378 In figure 9, wall-normal profiles of root-mean-square (r.m.s.) streamwise and crosswise
 379 velocities, $u_{r.m.s.}$ and $v_{r.m.s.}$, scaled with inner variables, with U_e , and with the Zaragola-
 380 Smits scaling $U_{ZS} = U_e\delta^*/\delta$ are shown for the four sensor locations, compared with the
 381 ZPG data of Spalart (1988) and both the ZPG and APG data of Na & Moin (1998) and
 382 Cohen & Gloerfelt (2018). Figures 9 (a,b) show profiles of $u_{r.m.s.}$ and $v_{r.m.s.}$ normalized
 383 by u_τ . A slightly higher peak for $u_{r.m.s.}^+$ in sensors 7 and 9 in comparison to Spalart (1988)
 384 can be attributed to the FPG region prior to those streamwise locations. The higher $u_{r.m.s.}^+$
 385 and $v_{r.m.s.}^+$ in APG region than in ZPG region is mainly because of the decrease of wall
 386 friction (figure 5). The smaller wall friction in the present DNS than in the reference studies
 387 (associated with stronger APG herein) also explains the larger $u_{r.m.s.}^+$ and $v_{r.m.s.}^+$ peaks
 388 in the present study. The inner peak elevations remain almost unchanged. Yet, a second
 389 peak forms in the outer layer in the $u_{r.m.s.}$ profile. The differences between the outer-peak
 390 locations (in wall units) in the present case and in the studies of Na & Moin (1998) and
 391 Cohen & Gloerfelt (2018) are most likely attributed to a combination of differences in APG,
 392 Reynolds number, and wall curvature. An effect of Reynolds number on the outer-layer peak
 393 location was discussed by Lee & Sung (2008) for instance. In figures 9 (c,d), the outer-layer
 394 velocity fluctuations normalized by U_e display large deviation from each other, and only
 395 collapse at the boundary-layer edge. However, when the APG cases are normalized by U_{ZS}
 396 (figures 9 (e,f)), the outer-layer velocity fluctuations are almost collapsed. This suggests that
 397 the Zaragola-Smits scaling applies to the outer portion of the boundary layer even under
 398 strong APG as in the present flow. This is consistent with the self-similarity in the outer
 399 region of APG TBL found by Maciel *et al.* (2006), Cohen & Gloerfelt (2018), and also
 400 verified by Rozenberg *et al.* (2012) to develop their semi-empirical model of wall-pressure
 401 fluctuations.

402 The wall-normal profiles of Reynolds shear stress in inner scaling at the four streamwise
 403 locations are plotted in figure 10. In the ZPG region, the profiles compare well with that
 404 of Spalart (1988); the same is observed for the u' and v' intensities (figure 9 (a,b)). The
 405 peaks of the Reynolds shear stress shift away from the wall in the APG region, moving into
 406 the logarithmic layer and even toward the edge of the outer region. This indicates enhanced
 407 turbulent mixing at locations farther away from the wall (Wu *et al.* 2019; Monty *et al.* 2011;
 408 Vila *et al.* 2017). As discussed by Lee & Sung (2008), who analyzed the effect of APG with
 409 similar Re_θ , the plateau seen so far for the strongest APG for y^+ between 10 and 50 may be
 410 due to the hairpin-type vortices developing away from the wall next to the TE region, also
 411 seen in the present DNS in figure 11, which shows the swirling strength criterion (Λ_{ci}) in the
 412 mid-chord (ZPG) region and near the trailing edge (APG region). A forest of large hairpin
 413 structures are shown to be lifted by the strong APG (see white dotted lines). Therefore, the

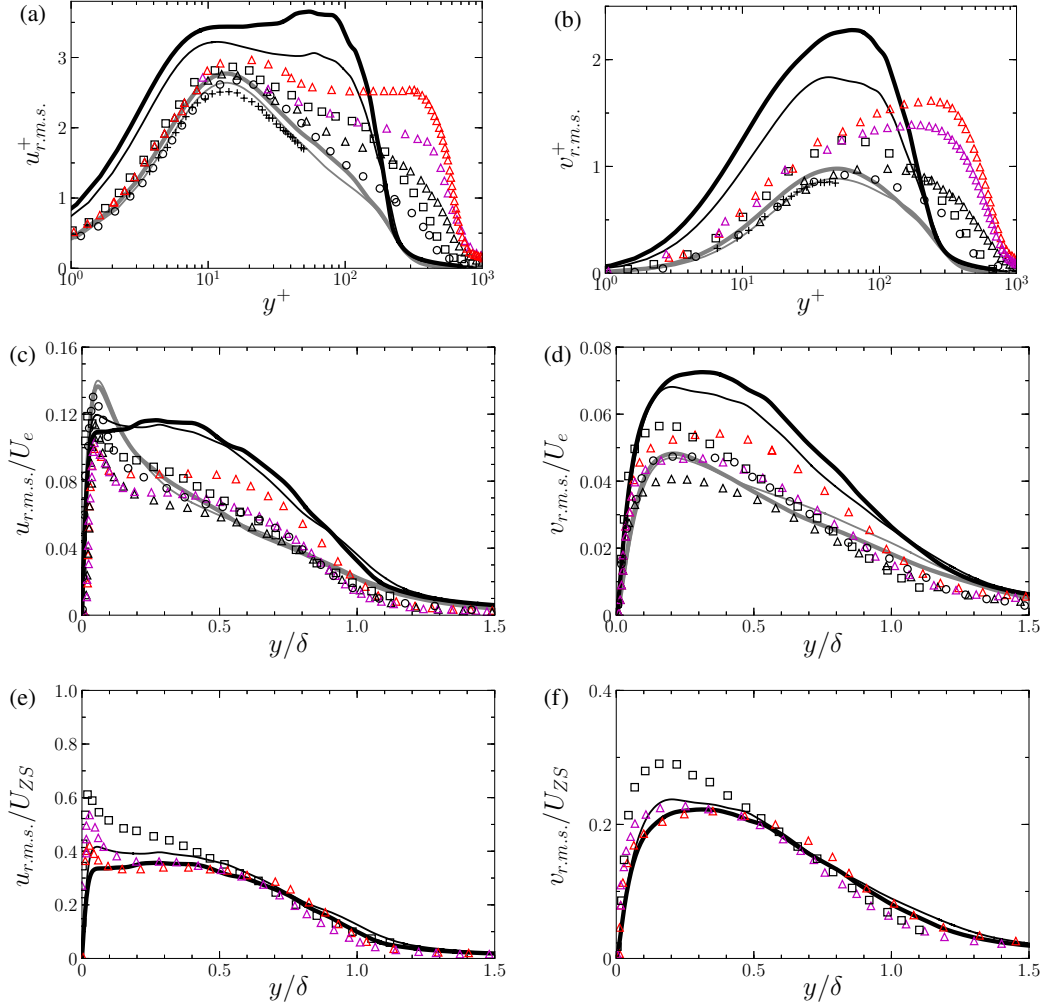


Figure 9: Comparison of r.m.s. velocities $u_{r.m.s.}$ and $v_{r.m.s.}$, in the wall-normal direction: (a-b) u_{τ} scaling; (c-d) U_e scaling; (e-f) $U_{ZS} = U_e \delta^*/\delta$ scaling. ZPG locations $x/c = -0.60$ (thin gray line) and $x/c = -0.47$ (thick gray line); APG locations $x/c = -0.14$ (thin black line), $x/c = -0.08$ (thick black line). +, ZPG data by Spalart (1988) with $Re_{\theta} = 300$; o, ZPG data $x = 0.5$ m, \square , APG data $x = 0.85$ m, for attached TBL (black) by Na & Moin (1998); \triangle , ZPG (black), APGs (red), APGw (magenta) data by Cohen & Gloerfelt (2018).

414 APG, characterized by a different momentum distribution mechanisms across the boundary
 415 layer, considerably affects the turbulent flow statistics (figure 10).

416 The results above show that boundary layer characteristics and single point velocity
 417 statistics at the four sensor locations are consistent with existing results in the literature.
 418 The agreements are quantitative at the ZPG locations. Overall, the peak location of the
 419 turbulent statistics and the wall-normal profiles are comparing very well with Spalart
 420 (1988) (see gray lines up to $y^+ \approx 60$ in figures 9 and 10). The agreement is qualitative at the
 421 APG locations because of the different Reynolds numbers, pressure gradients and wall curvature.
 422 Interestingly, the self-similarity in the outer region of the boundary layer provided by the
 423 Zagarola-Smits scaling is verified in the present strong non-equilibrium TBL, suggesting that

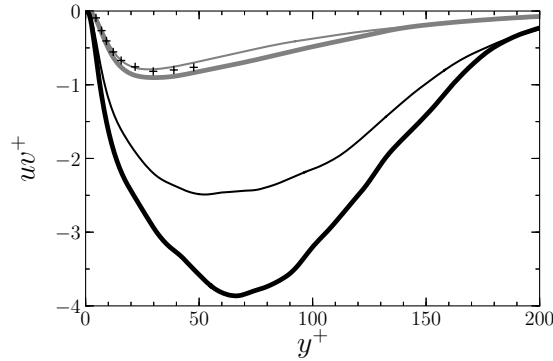


Figure 10: Reynolds stress component normalized with inner scale along wall-normal direction: ZPG locations $x/c = -0.60$ (thin gray line) and $x/c = -0.47$ (thick gray line); APG locations $x/c = -0.14$ (thin black line), $x/c = -0.08$ (thick black line). +, ZPG data by Spalart (1988) with $Re_\theta = 300$.

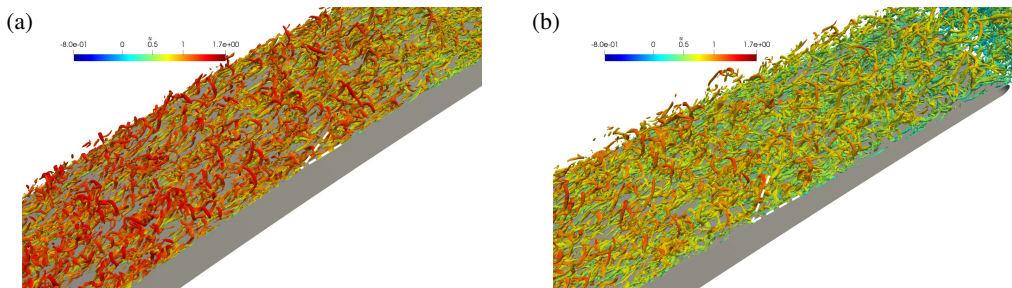


Figure 11: Swirling strength criterion (Zhou *et al.* 1999; Wu *et al.* 2017) isocontours coloured by streamwise velocity component by Wu *et al.* (2019): (a) ZPG portion (mid-chord) and (b) APG (or TE) portion.

424 the Zaragola-Smits velocity might be a relevant velocity scale for all attached TBL. The above
 425 discussion on variation of boundary layer parameters will serve as a guide on normalizing
 426 wall pressure statistics. For instance, turbulence statistics—when made dimensionless by
 427 Zaragola-Smits scaling—gives a collapse in outer region, and thus may serve as an optimal
 428 velocity scale to collapse low frequency wall-pressure spectra. The development of boundary
 429 layer thicknesses discussed in figure 6 can also guide in choosing the correct normalizing
 430 length scale for wall pressure spectra in highly nonequilibrium cases. Moreover, the high
 431 sensitivity of C_f to APG, more aptly wall shear, suggests that it may not be an optimal
 432 parameter to non-dimensionalize pressure fluctuations, even though most semi-empirical
 433 models for wall-pressure spectra use it as a pressure scale. This will be shown in detail in the
 434 next section.

435 4. Wall-pressure statistics

436 Statistics of the wall-pressure field on the surface of the CD aerofoil particularly relevant
 437 to trailing-edge noise modelling are presented here. PSD, two-point correlation, coherence
 438 functions, wavenumber-frequency spectra and convection velocity are discussed at the four
 439 locations corresponding to sensors 7, 9, 21 and 24. They are compared with available data
 440 (Choi & Moin 1990; Na & Moin 1998; Spalart 1988; Abe *et al.* 2005; Cohen & Gloerfelt
 441 2018; Burton 1973; Simpson *et al.* 1987; Skote *et al.* 1998; Schewe 1983).

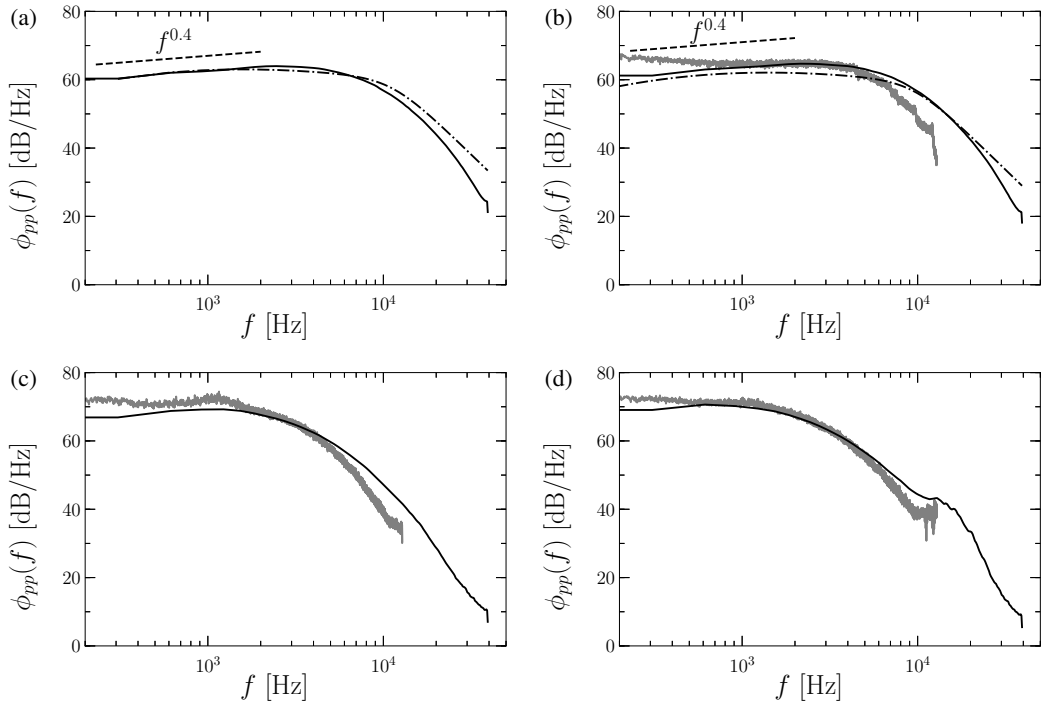


Figure 12: Spanwise-averaged wall-pressure spectra at four locations on the aerofoil suction side: —, DNS-NS; - - -, Goody's model and, — (gray), UdeS measurements. (a) $x/c = -0.60$, (b) $x/c = -0.47$, (c) $x/c = -0.14$ and (d) $x/c = -0.08$.

442

4.1. Power Spectral Density distribution

443 The PSD of the wall-pressure fluctuations at a given frequency, $\phi_{pp}(f)$, is calculated from the
 444 wall-pressure CSD, as defined in section 2.1. The spanwise-averaged wall-pressure spectra
 445 in decibels with respect to the reference pressure 2×10^5 Pa for a spectral resolution of
 446 1 Hz (dB/Hz in short) are shown in figure 12 for the four locations on the aerofoil suction
 447 side indicated in figure 1. The PSD calculated from DNS are compared to the available
 448 experimental data from UdeS measurements (Jaiswal *et al.* 2020; Jaiswal 2020). Note that the
 449 experimental results for sensor 7 are missing because of a microphone failure. In figures 12 (a,
 450 b), for the ZPG regions 7 and 9, the semi-empirical spectrum defined by Goody (2004) is
 451 also represented. Such a model compares well with experimental data over a large range of
 452 Reynolds numbers (Hwang *et al.* 2009), and is able to describe the essential properties of the
 453 single-point wall-pressure spectrum for ZPG boundary layers based on a limited numbers
 454 of variables. Note that at low frequencies, the same -0.4 slope is recovered as observed
 455 in the APG DNS of Na & Moin (1998). For sensor 24 (figure 12 (d)) the DNS spectrum
 456 shows a small hump around 10 kHz. This hump in the higher frequency range is also seen
 457 in the experimental data (gray line) and corresponds to an extra acoustic source in the wake
 458 (Wu *et al.* 2020). Going towards the trailing edge, there is an increase in spectral levels of
 459 approximately 10 dB/Hz at the low frequencies, and a faster roll-off decrease towards high
 460 frequency. This is an APG effect, also observed in previous studies (Na & Moin 1998; Cohen
 461 & Gloerfelt 2018). In the low-frequency range a plateau below 500 Hz is seen for sensors
 462 21 and 24, while sensors 7 and 9 show the characteristic ZPG quadratic rise with frequency
 463 following Goody's empirical model. Overall, the DNS and experimental results are in good

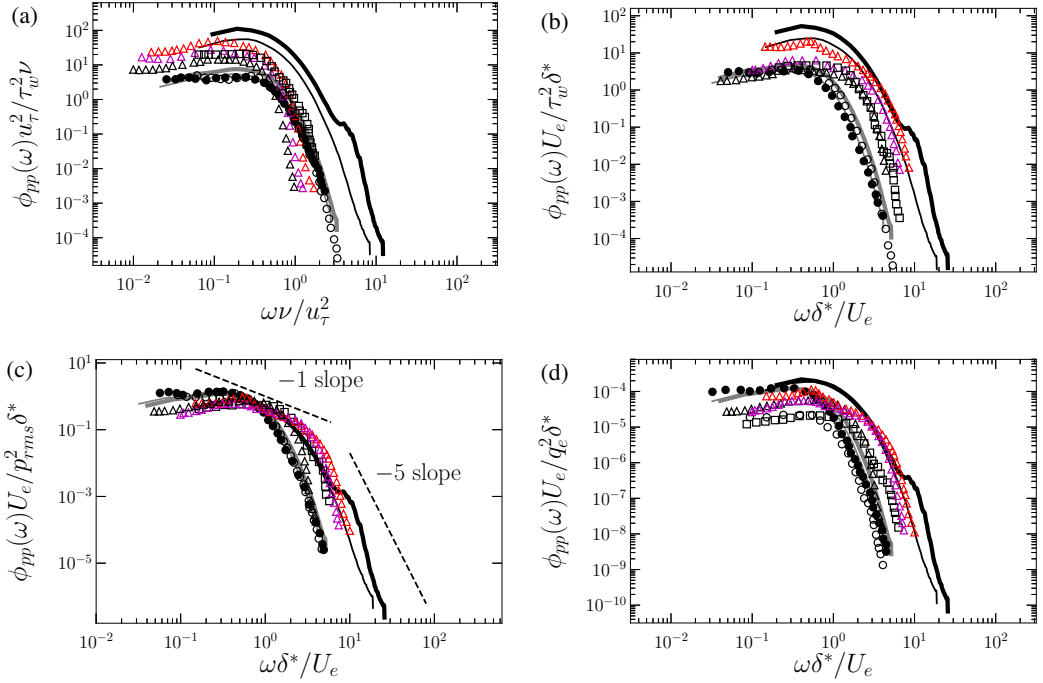


Figure 13: Dimensionless spanwise-averaged wall-pressure spectra at four locations on the aerofoil suction side: (a) Inner variables scaling, (b) mixed inner-outer variables scaling and (c-d) outer variables scaling. ZPG locations $x/c = -0.60$ (thin gray line) and $x/c = -0.47$ (thick gray line); APG locations $x/c = -0.14$ (thin black line), $x/c = -0.08$ (thick black line); \bullet , data by Choi & Moin (1990); \circ , ZPG data $x = 0.5$ m, and \square , APG data $x = 0.85$ m for attached TBL by Na & Moin (1998); \triangle , ZPG (black), APGs (red), APGw (magenta) data by Cohen & Gloerfelt (2018).

464 agreement. The difference of PSDs between numerical and experimental results in the low-
 465 frequency range, approximately under 500 Hz, is most likely related to installation effects,
 466 either attributed to jet noise (Moreau *et al.* 2003) or to the unsteady interaction between the
 467 jet shear layer and the aerofoil, as well as the low background turbulence intensity (less than
 468 0.4 %) seen in the experiments (Padois *et al.* 2015) and not included in this DNS (Wu *et al.*
 469 2020).

470 In order to deduce the main contributors to the wall-pressure fluctuations in different
 471 frequency bands, the PSD and the frequency are then normalized based on several inner,
 472 outer and mixed scalings in figure 13. Different normalizations have been proposed over the
 473 years (Bull 1996; Keith *et al.* 1992; Farabee & Casarella 1991; Choi & Moin 1990; Cipolla
 474 & Keith 2000; Schloemer 1967; Na & Moin 1998). There is not a single universal scaling
 475 that leads to an acceptable collapse of data in the entire frequency range due to the multiscale
 476 nature of turbulence. However, as observed by Bull (1996) for ZPG flows, the wall-pressure
 477 fluctuations at low frequencies originate predominately from the outer layer, while those
 478 at high frequencies—where the spectrum varies as ω^{-5} (Gravante *et al.* 1998; Na & Moin
 479 1998; Moreau & Roger 2005)—originate mostly from the buffer layer. Consequently, the
 480 wall-pressure PSD scales on outer variables at lower frequencies and inner variables at high
 481 frequencies. In the mid-frequency range, a scale-independent overlap region exists, where the
 482 PSD is proportional to ω^{-1} (Bradshaw 1967; Gravante *et al.* 1998). This range is associated
 483 with motions in the logarithmic region.

484 The best inner variable scaling for the high-frequency range has been found by plotting
 485 $\phi_{pp}(\omega)u_\tau^2/\tau_w^2\nu$ versus $\omega\nu/u_\tau^2$ and is used in figure 13 (a). For the mid-frequency range, a
 486 satisfactory data collapse is usually obtained by scaling $\phi_{pp}(\omega)$ using the mixed inner-outer
 487 variables, U_e , δ^* and τ_w , with dimensionless frequency $\omega\delta^*/U_e$ (Keith *et al.* 1992; Choi &
 488 Moin 1990; Na & Moin 1998). This is shown in figure 13 (b). Finally, in figures 13 (c,d),
 489 common outer variable scalings for the low-frequency range are used: $\phi_{pp}(\omega)U_e/p_{rms}^2\delta^*$
 490 and $\phi_{pp}(\omega)U_e/q_e^2\delta^*$, both versus $\omega\delta^*/U_e$ (Choi & Moin 1990; Na & Moin 1998). Here, q_e
 491 is the dynamic pressure at the edge of the boundary layer.

492 First, the focus is given to the ZPG data sets. Normalization with inner variables (figure 13
 493 (a)) collapses the spectra at high frequencies as expected, consistently with the findings of
 494 Na & Moin (1998) and Choi & Moin (1990). Moreover, the present spectra at sensors 7 and
 495 9 collapse well in the whole spectral range with that of Choi & Moin (1990), as the flow
 496 is characterized by a similar range of Re_θ (see table 1). In figure 13 (b), the scaling with
 497 $U_e/\tau_w^2\delta^*$ gives an overall collapse at low to mid frequencies, which was also observed by Na
 498 & Moin (1998), Choi & Moin (1990) and Cohen & Gloerfelt (2018). In addition, the effect
 499 of Reynolds numbers on the PSD is shown. As observed by Goody (2004), the main effect
 500 of Reynolds number on the wall-pressure spectrum is to widen its overlap range and shift the
 501 roll-off towards higher frequencies. This is indeed shown in figure 13 (c,d), comparing data
 502 from Cohen & Gloerfelt (2018) with those from Choi & Moin (1990) and those from sensor
 503 7 to those from sensor 24 at a higher Reynolds number, for example. This is caused by the
 504 widening of the spectrum of turbulent motions and a larger logarithmic region associated
 505 with a higher-Reynolds-number boundary layer. Furthermore, a region of the spectra with a
 506 -5 slope in the high-frequency range, linked to the turbulent motions inside the buffer zone,
 507 is also shown in figure 13 (c).

508 As the pressure gradient changes from zero to adverse (from sensor 9 to sensor 24), an
 509 overall increase in spectral levels normalized by the inner velocity scale is seen in figure 13,
 510 suggesting an augmentation of wall-pressure r.m.s. due to the APG, relative to u_τ . In the
 511 presence of an APG the inner variables normalization does not collapse the spectra at high
 512 frequencies, consistently with the observations of Na & Moin (1998) and Cohen & Gloerfelt
 513 (2018). This is because of the decrease in wall shear stress under APG. When the spectra
 514 are normalized by wall-pressure r.m.s. and δ^* (figure 13 (c)), a collapse in the low to mid
 515 frequency range is seen. This is expected since p_{rms}^2 represents the integral of the spectrum.
 516 The scaling with local dynamic pressure (figure 13 (d)), on the other hand, does not give
 517 a good collapse in the low to mid frequency range, which is consistent with what Brooks
 518 & Hodgson (1981) observed on the NACA0012 aerofoil (figure 11 in Brooks & Hodgson
 519 (1981)). This is because the APG leads to augmentation of wall-pressure fluctuations at
 520 low frequencies, while it is associated with free-stream deceleration, i.e. a reduction in the
 521 edge dynamic pressure. Na & Moin (1998) also observed similar comparison between ZPG
 522 and APG wall-pressure spectra for the normalizations analyzed herein. Given that all cases
 523 plotted here differ in Reynolds numbers, pressure gradients and wall curvature, the spectra
 524 do not overlap over the entire frequency range. In addition, both ZPG and APG data of
 525 Cohen & Gloerfelt (2018) display a faster roll-off at high frequencies, which is most likely a
 526 consequence of the spatial cut-off of the LES. **These results also indicate that scalings used
 527 in popular semi-empirical models, especially using wall shear stress as the pressure scale,
 528 may be inappropriate for strong-APG flows.**

529 In figure 14, the pressure spectra are plotted again normalized using δ instead of δ^* ,
 530 which is equivalent to using the Zaragoza-Smits scaling instead of U_e in figure 13 (since
 531 $\omega\delta/U_e = \omega\delta^*/U_{ZS}$ and $U_e/\delta = U_{ZS}/\delta^*$). **ZPG and APG data of Cohen & Gloerfelt (2018)
 532 for which all parameters are available are also shown.** As shown by figure 6(b,c) and also

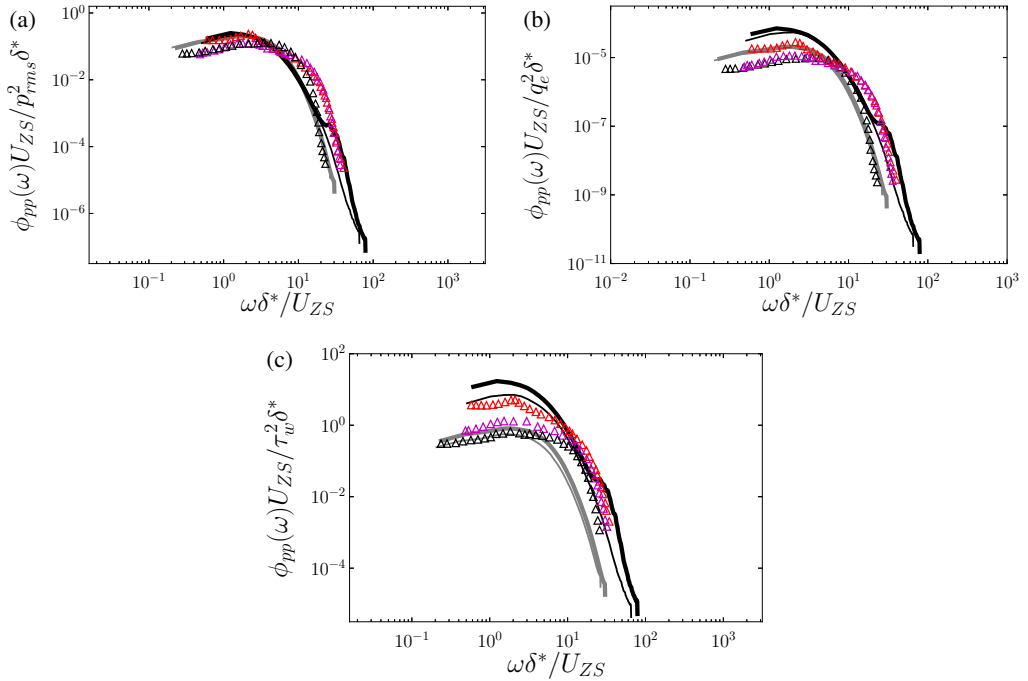


Figure 14: Spanwise-averaged wall-pressure spectra at four locations on the aerofoil suction side scaled with Zaragola-Smits scaling, $U_{ZS} = U_e \delta^* / \delta$: ZPG locations $x/c = -0.60$ (thin gray line) and $x/c = -0.47$ (thick gray line); APG locations $x/c = -0.14$ (thin black line), $x/c = -0.08$ (thick black line); Δ , ZPG (black), APGs (red), APGw (magenta) data by Cohen & Gloerfelt (2018). (a-b) Outer and (c) mixed inner-outer variables scaling.

533 indicated by Keith *et al.* (1992) and Farabee & Casarella (1991), δ and δ^* are not equivalent
 534 length scales given that their ratio varies with Reynolds number. For the outer scaling, both
 535 figures 14 (a,b) show a significantly improved collapse compared with figures 13 (c,d).
 536 This indicates that δ is a better length scale in the low- to mid-frequency range than δ^* ,
 537 or equivalently that U_{ZS} is a better velocity scale than U_e . Similarly, for the mixed inner-
 538 outer variable scaling, figure 14 (c) shows a slightly better merge of the normalized spectra
 539 at mid-to-high frequencies for both ZPG and APG regions than in figure 13 (b). Finally,
 540 the best overall collapse of normalized spectra in the whole frequency range is found in
 541 figure 14 (a), which stresses that p_{rms} is a better pressure scale than q_e for the present highly
 542 non-equilibrium TBL. Hence, in development of wall pressure spectra models, more focus
 543 is needed on modelling pressure gradient effects on p_{rms} or on variables that scale with it.

544 In figure 15 (a), the wall-pressure r.m.s. normalized by ρU_{in}^2 (where U_{in} is taken equal to
 545 the edge velocity at sensor 7) as a function of wall-normal distance is compared with that
 546 of Na & Moin (1998), for both attached and separated TBLs. Three different TBL cases by
 547 Na & Moin (1998) are also considered, characterized respectively by ZPG at $x/\delta_{in}^* = 80$,
 548 a weak APG at $x/\delta_{in}^* = 120$, and a stronger APG just after the detachment at $x/\delta_{in}^* = 160$
 549 therein. A local maximum of p_{rms} is seen and both its elevation and magnitude increase as
 550 the flow moves downstream (with strengthened APG) in accordance with the trend shown
 551 by Na & Moin (1998). Close to the trailing edge (sensors 21 and 24) the levels and the
 552 hump size are close to those near the onset of separation in the flow studied by Na & Moin
 553 (1998) ($x/\delta_{in}^* = 160$), highlighting the high load of the present case, consistently with the

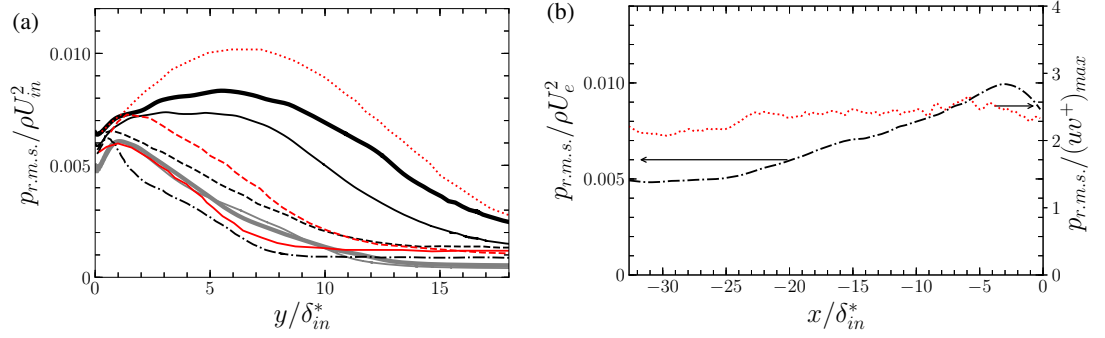


Figure 15: Root-mean-square values of (a) pressure fluctuations r.m.s. along wall-normal direction and (b) streamwise distribution of the wall-pressure r.m.s. normalized with local Reynolds shear stress ($\cdot\cdot\cdot$) or dynamic pressure ($- - -$). ZPG locations $x/c = -0.60$ (thin gray line) and $x/c = -0.47$ (thick gray line); APG locations $x/c = -0.14$ (thin black line), $x/c = -0.08$ (thick black line). Na & Moin (1998) data: $\cdot\cdot\cdot$, ZPG data at $x = 0.5$ m, $- -$, APG data at $x = 0.85$ m for attached TBL (black); $—$, $x/\delta_{in}^* = 80$, $- -$, $x/\delta_{in}^* = 120$, $\cdot\cdot\cdot$, $x/\delta_{in}^* = 160$ for separated TBL (red).

554 shape factor seen in figure 5 (c) and in table 1. The streamwise increase of the pressure
 555 fluctuations at the wall is also seen in figure 15 (b), which shows the streamwise distribution
 556 of the wall-pressure r.m.s. normalized by the local maximum magnitude of Reynolds shear
 557 stress or the local dynamic pressure. There is clearly less streamwise variation of the wall-
 558 pressure r.m.s. when normalized with local peak Reynolds shear stress, as also shown by Na
 559 & Moin (1998). Thus, the peak Reynolds shear stress magnitude could be a better scaling
 560 variable for wall-pressure fluctuations than U_e^2 for all APG flows including the present strong
 561 non-equilibrium TBL case.

562 In figures 16 (a,b) the root-mean-square values of the wall-pressure scaled with τ_w or the
 563 dynamic pressure versus the friction Reynolds number, $Re_\tau = u_\tau \delta / \nu$, are shown at the four
 564 locations. In figure 16 (c), the CD aerofoil distribution of p_{rms}^+ is also plotted versus the
 565 momentum thickness based Reynolds number. ZPG data of Choi & Moin (1990), DNS data
 566 of Abe *et al.* (2005), and ZPG data of Spalart (1988), Cohen & Gloerfelt (2018), Skote *et al.*
 567 (1998) and Schewe (1983) are considered for comparison of ZPG data. The empirical law of
 568 p_{rms}^+ versus Re_τ developed for ZPG flows by Farabee & Casarella (1991) is also plotted in
 569 figure 16 (a), in which $(p_{rms}^+)^2 = 6.5 + 1.86 \ln(Re_\tau/333)$ for $Re_\tau > 333$ and $(p_{rms}^+)^2 = 6.5$
 570 for $Re_\tau \leq 333$. For APG flows, data of Cohen & Gloerfelt (2018), Simpson *et al.* (1987) and
 571 Burton (1973) are compared here. The data show that p_{rms}^+ weakly increases with Re_τ in ZPG
 572 flows following the empirical law proposed by Farabee & Casarella (1991). For APG flows,
 573 a greater scatter is observed, particularly in figure 16 (a) (see APG locations $x/c = -0.14$
 574 and $x/c = -0.08$ in the present flow and strong-APG data of Burton (1973) and Simpson
 575 *et al.* (1987)). APG leads to higher p_{rms}^+ than in a ZPG flow at the same Reynolds number. In
 576 comparison, less scatter is observed in figure 16 (b), indicating a better correlation between
 577 the wall-pressure r.m.s. and the edge dynamic pressure than that with τ_w . Finally, the sharp
 578 increase in p_{rms} with x seen in figure 16 for the present aerofoil further confirms the strong
 579 non-equilibrium state of the boundary layer at the trailing edge, subject to a sharp APG.

580 In summary, the usual inner or inner-outer variable scalings are seen to work in the ZPG
 581 regions of the CD aerofoil (despite the possible history effects of the upstream FPG region),
 582 but not in the APG regions, with larger departures for higher β_c , as found in previous studies.
 583 The best scaling parameters are found to be the outer variables U_e , δ and p_{rms} or equivalently

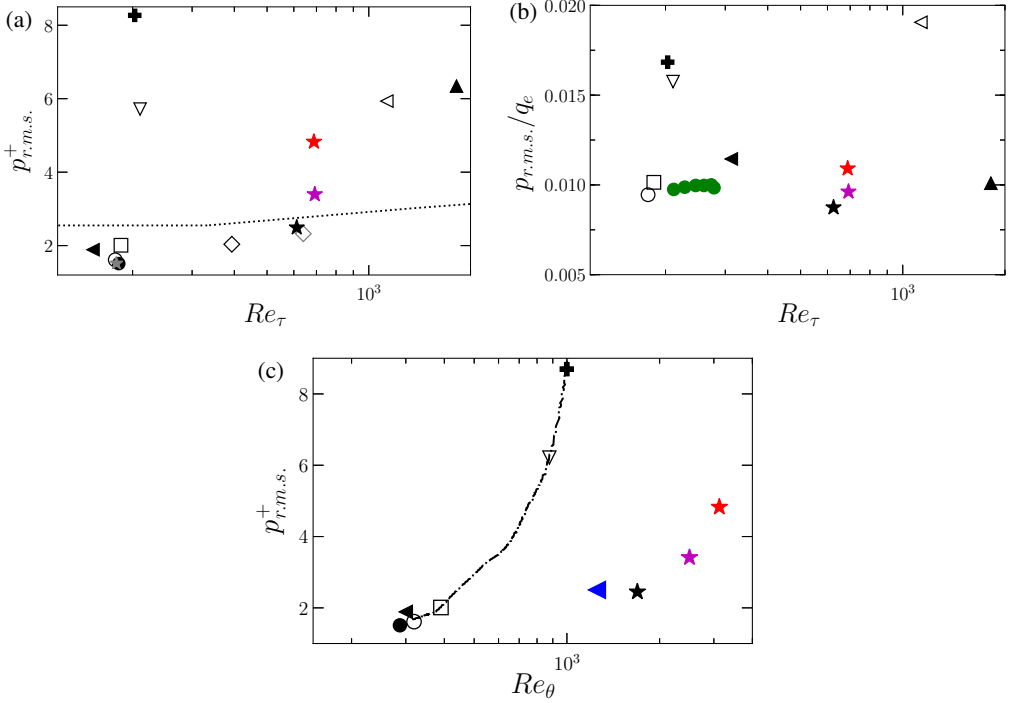


Figure 16: Root-mean-square values of the wall-pressure r.m.s.: (a) τ_w scaling and (b) dynamic pressure scaling versus the friction Reynolds number; (c) τ_w scaling versus the momentum thickness based Reynolds number. ZPG locations \circ , $x/c = -0.60$ and \square , $x/c = -0.47$; APG locations ∇ , $x/c = -0.14$ and $+$, $x/c = -0.08$; \bullet , Choi & Moin (1990)'s data; Abe *et al.* (2005)'s data (\star , $Re_\tau = 180$; \diamond , $Re_\tau = 395$; \diamond , $Re_\tau = 640$); \blacktriangleleft , Spalart (1988)'s data; \star , ZPG (black), APGs (red), APGw (magenta) data by Cohen & Gloerfelt (2018); \blacktriangleleft , Simpson *et al.* (1987) APG's data; \blacktriangle , Burton (1973) APG's data; \dots , empirical law from Farabee & Casarella (1991); \bullet (green), ZPG data by Skote *et al.* (1998) $Re_\theta = 350 - 525$; $-\cdot-$ CD aerofoil distribution; \blacktriangleleft (blue) data by Schewe (1983).

584 U_{ZS} , δ^* and p_{rms} . This indirectly stresses that the overall wall-pressure fluctuations are
585 dominated by the large turbulent scales, the contribution of which increases with higher β_c .
586 In turn, p_{rms} is seen to scale more with outer variables such as the dynamic pressure q_e than
587 with inner scales such as τ_w . As found previously by Na & Moin (1998) and Abe (2017) for
588 instance, a quasi invariant is obtained when scaling p_{rms} with the local maximum Reynolds
589 shear stress magnitude for the whole range of Reynolds number considered here in a strong
590 non-equilibrium turbulent boundary layer typical of low-speed rotating machines. **This has**
591 **an important implication in choosing correct scalings in WPS models. For instance, most**
592 **models use the wall shear stress as the pressure scale. However, our results show that p_{rms}**
593 **or the peak Reynolds shear stress magnitude are more appropriate low-frequency pressure**
594 **scales. Another important finding is that, for low Reynolds number cases such as the current**
595 **one, using δ and U_e as length and velocity scales may give good overall collapse of wall**
596 **pressure spectra, as shown in figure 14 (a).**

597

4.2. Two-point correlations and coherence functions

598 The contour plots of the two-point correlation functions of wall-pressure fluctuations,
599 introduced in section 2.1, are shown in figure 17 as a function of streamwise (ξ_x) and

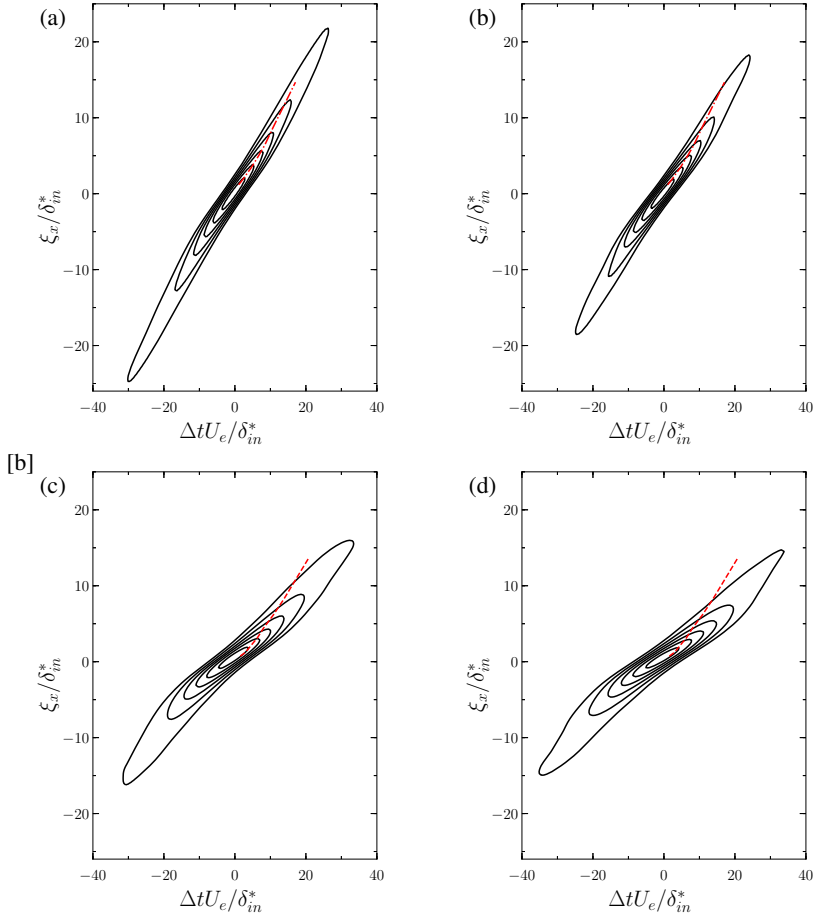


Figure 17: Contour plot of two-point correlation of wall-pressure fluctuations versus streamwise spatial and temporal separations. Contour levels are from 0.15 to 0.9 with increments of 0.15. (a) $x/c = -0.60$; (b) $x/c = -0.47$; (c) $x/c = -0.14$; and (d) $x/c = -0.08$. Red lines are collections of outermost point of each iso-contour line for the attached TBL by Na & Moin (1998) to indicate inclinations of the iso-contours: $\cdot - \cdot -$ (red), ZPG data at $x = 0.5$ m and $--$ (red), APG data at $x = 0.85$ m.

600 temporal (Δt) separations and normalized with inlet parameters. The slope $d(\xi_x)/d(\Delta t)$ gives
 601 the propagation speed of the eddies, the signatures of which are reflected in wall-pressure
 602 fluctuations. As a reference, these slopes of the cross-correlation at each spatial separation
 603 found in Na & Moin (1998) flat-plate case of attached TBL, with ZPG at $x = 0.50$ m and with
 604 APG at $x = 0.85$ m, are also indicated by dotted-dashed and dashed red lines, respectively.
 605 As expected, a larger propagation speed is seen in the ZPG region, while in the APG region
 606 the convection speed of the turbulent structures is reduced and the contour plots are broader
 607 This is associated with a longer correlation time of wall pressure fluctuations in APG region,
 608 and it suggests a lower convection velocity of turbulent structures, which will be discussed
 609 later. Variations of both the slope and broadness of the contours with APG are in agreement
 610 with the observations of Na & Moin (1998), despite different Re_θ ranges and a stronger APG
 611 reached in the present flow.

612 By Fourier transforming the two-point correlation function, the CSD $\Psi_{pp}(\xi; \omega)$ is

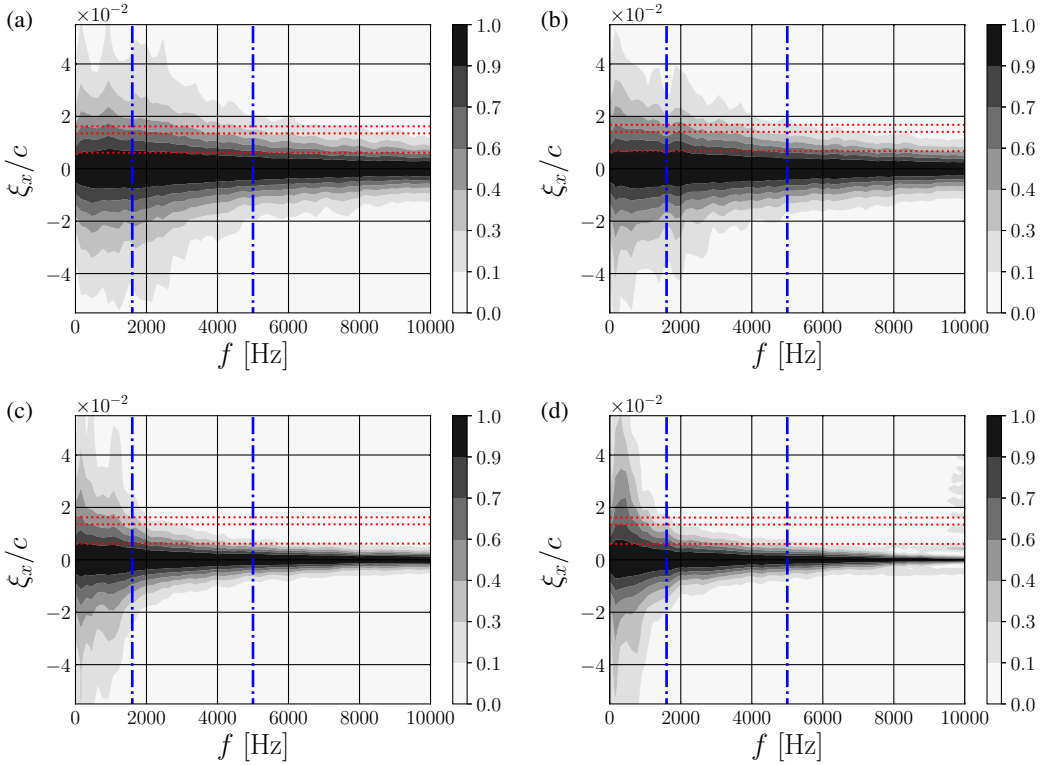


Figure 18: Contours of streamwise coherence of fluctuating pressure for ZPG and APG regions: (a) $x/c = -0.60$; (b) $x/c = -0.47$; (c) $x/c = -0.14$; and (d) $x/c = -0.08$ (red) spatial separations $\xi_x/c = 0.007, 0.013, 0.016$ used in figures 20 and 21; - - - (blue) frequencies of 1600 and 5000 Hz used in figures 22 and 23.

613 calculated (see section 2.1). The cross-spectrum $\Psi_{pp}(\xi; \omega)$ is useful for studying the wall-
 614 pressure spatial coherence as a function of frequency (Moreau & Roger 2005; Roger &
 615 Moreau 2005). In general, the coherence function between two points on the aerofoil surface
 616 can be defined as:

$$617 \quad \gamma^2(\xi; \omega) = \frac{|\Psi_{pp}(\xi; \omega)|^2}{\phi_{pp}(\omega)^2}. \quad (4.1)$$

618 The coherence function describes the correlation between two points with a spatial separation
 619 of ξ_x in the longitudinal (or streamwise) direction and ξ_z in the lateral (or spanwise) direction
 620 at a given frequency. The contours of the calculated coherence distributions are shown along
 621 the streamwise and spanwise directions in figures 18 and 19, respectively. On the one
 622 hand, both streamwise and spanwise coherence functions are not seen to vary much in the
 623 ZPG regions, with a larger coherence in the streamwise direction. On the other hand, the
 624 streamwise coherence is seen to be reduced by APG for the whole frequency range, while
 625 the spanwise coherence overall increases with APG, especially at low frequencies, as already
 626 noted by Wang *et al.* (2009) based on the first LES on the present aerofoil. Figure 19 also
 627 indicates that the spanwise extent of the computational domain (i.e., $0.12 C$) is sufficient for
 628 proper flow development in both ZPG and APG regions for most frequencies beyond 200
 629 Hz, as already pointed out by Wang *et al.* (2009) and confirmed experimentally in several
 630 test facilities (Moreau & Roger 2005; Jaiswal *et al.* 2020; Jaiswal 2020). A slight increase

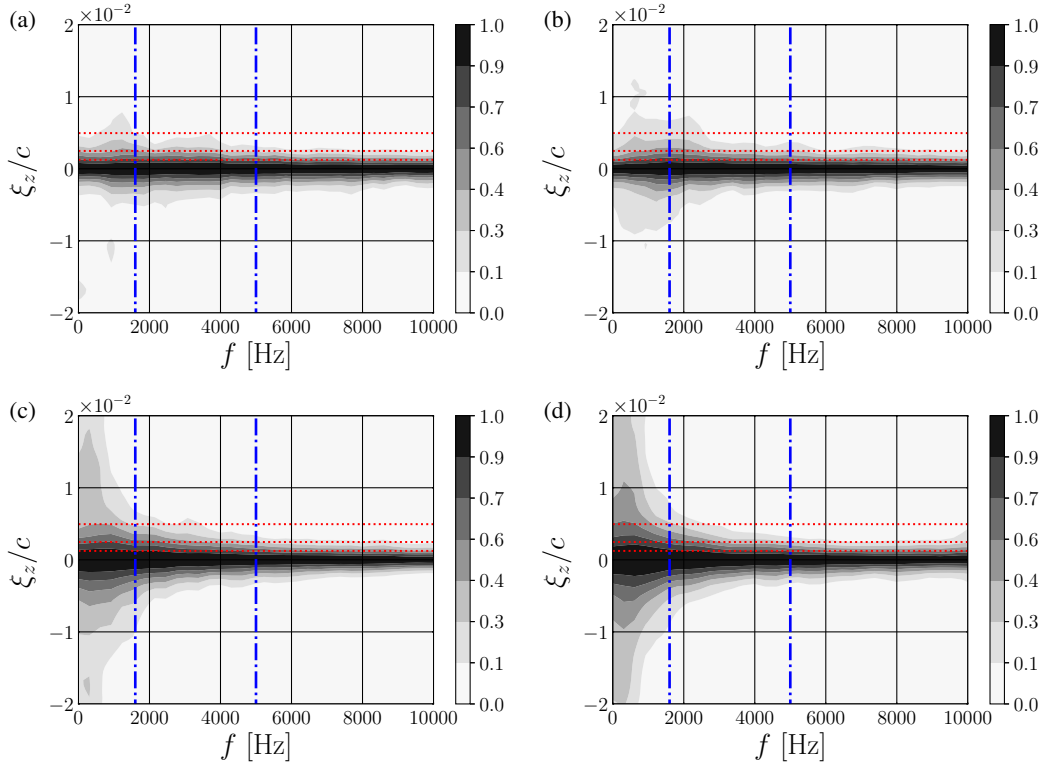


Figure 19: Contours of spanwise coherence of fluctuating pressure for ZPG and APG regions: (a) $x/c = -0.60$; (b) $x/c = -0.47$; (c) $x/c = -0.14$; and (d) $x/c = -0.08$. \dots (red), spatial separations $\xi_z/c = 0.0019, 0.0025, 0.0049$ used in figures 20 and 21; $-\cdot-\cdot$ (blue) frequencies 1600 and 5000 Hz used in figures 22 and 23.

631 of coherence level in the high frequency range is found for sensor 24, which is caused
 632 by an acoustic contamination by an extra noise source in the wake, as already seen in the
 633 wall-pressure PSD in figures 12 to 14 and as mentioned by Wu *et al.* (2020).

634 More quantitative estimates are provided by the magnitudes of the normalized
 635 longitudinal and lateral CSD, $\gamma(\xi_x, \omega) = |\Psi_{pp}(\xi_x, 0, \omega)|/\phi_{pp}(\omega)$ and $\gamma(\xi_z, \omega) =$
 636 $|\Psi_{pp}(0, \xi_z, \omega)|/\phi_{pp}(\omega)$, respectively. First, figures 20 and 21 show these normalized CSD
 637 versus the normalized frequency $\omega\delta_{in}^*/U_\infty$ for different spatial separations, indicated with
 638 horizontal red dotted lines in figures 18 and 19. In figure 20, the normalized longitudinal
 639 CSD in APG is seen to be systematically below that for a ZPG, as already noticed
 640 by Schloemer (1967). The levels are higher at sensor 7 than at sensor 9, most likely a history
 641 effect of the upstream FPG flow. The decay of coherence with frequency is also seen to be
 642 faster in APG (with a power-law slope of -0.4) than in ZPG (with a slope of -0.32). In figure
 643 20, $\gamma(\xi_x, \omega)$ is also compared with distributions provided by Hu (2021), who measured
 644 wall-pressure fluctuations induced by TBL with different pressure gradients by installing a
 645 NACA0012 aerofoil above a flat plate with an adjustable angle of attack. Even though the
 646 Reynolds numbers Re_θ are much larger in the latter experiments, good agreement is found in
 647 the variation of streamwise coherence with frequencies for both ZPG and APG conditions.
 648 Only at high frequencies, a slightly faster decay in ZPG is seen in the distributions of Hu
 649 (2021), but the correlations are low and bear the largest experimental uncertainties. Such a
 650 good match underlines that the streamwise wall-pressure coherence is quite insensitive to

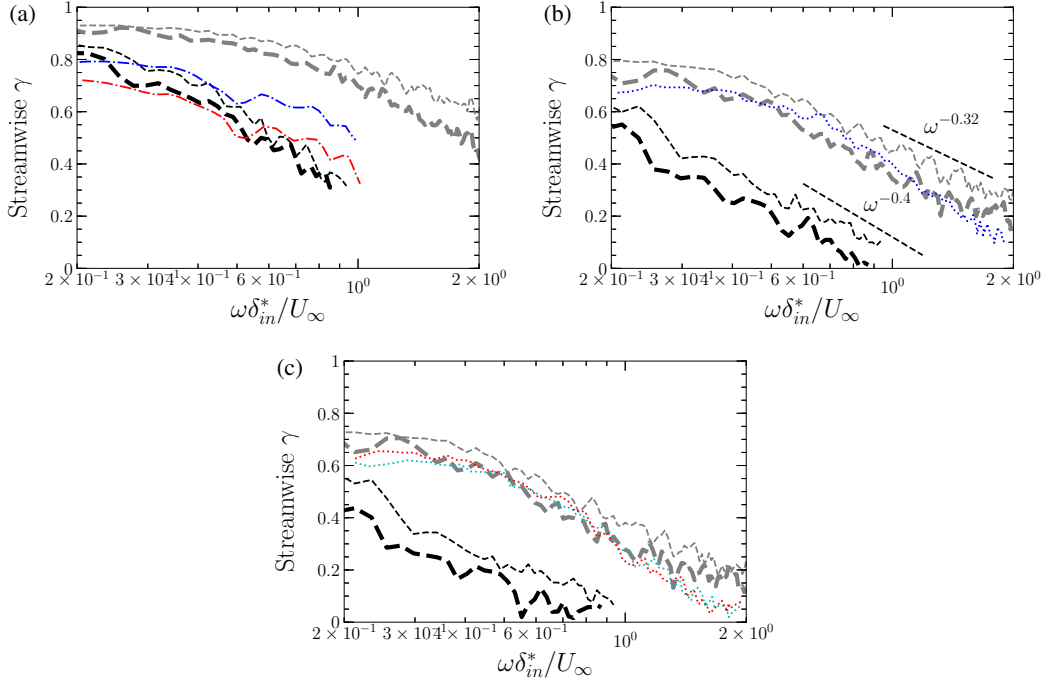


Figure 20: Streamwise $\gamma(\xi_x, \omega)$ frequency distribution for different spatial separations at four location on the aerofoil suction side: --, ZPG locations $x/c = -0.60$ (thin gray line) and $x/c = -0.47$ (thick gray line); --, APG locations $x/c = -0.14$ (thin black line), $x/c = -0.08$ (thick black line). \cdots ZPG data by Hu (2021) (blue for $\xi_x/\delta^* = 4.3$, red for $\xi_x/\delta^* = 6.0$ and turquoise for $\xi_x/\delta^* = 6.3$); $-\cdot-$ APG data by Hu (2021) (blue for $\xi_x/\delta^* = 2.0$ and red for $\xi_x/\delta^* = 2.7$). (a) $\xi_x/c = 0.007$ and $\xi_x/\delta_{in}^* = 2.61$; (b) $\xi_x/c = 0.013$ and $\xi_x/\delta_{in}^* = 5.19$; (c) $\xi_x/c = 0.016$ and $\xi_x/\delta_{in}^* = 6.23$.

651 a significant variation in Re_θ , similar to what was observed in the velocity correlations by
 652 Sillero *et al.* (2014) in ZPG TBL on flat plates and by Pargal *et al.* (2022) with the present
 653 DNS data of a CD aerofoil and with another DNS of flow on a flat plate with the same
 654 external mean pressure gradient. In figure 21, the normalized lateral CSD are seen to vary
 655 far less with flow conditions than the longitudinal ones. Only at low to mid frequencies,
 656 a systematic increase of spanwise coherence is observed with APG, consistently with the
 657 observations of Wang *et al.* (2009). **This coherence increase in a given frequency range is**
 658 **predominantly associated with large turbulent structures formed during APG.**

659 Next, figures 22 and 23 show the coherence, γ^2 , versus various streamwise and spanwise
 660 separations at two increasing frequencies, indicated with vertical blue dashed-dotted lines
 661 in figures 18 and 19, for the four locations on the aerofoil. A faster decay of coherence
 662 with distance (in both x and z) is observed for higher frequencies, regardless of the mean
 663 pressure gradient. The streamwise coherence in figure 22(a) decays rapidly with longitudinal
 664 distance when moving downstream, indicating shorter coherence in the APG region than in
 665 the ZPG one. However, the spanwise coherence decay with lateral distance in figure 23(b)
 666 does not show significant difference between the four chordwise locations. As also observed
 667 in Schloemer (1967), the **spanwise** coherence decays faster with distance than the **streamwise**
 668 one in both ZPG and APG regions for both frequencies. A similar trend was also found
 669 by Brooks & Hodgson (1981) on the NACA0012 aerofoil (figure 16 in (Brooks & Hodgson
 670 1981)).

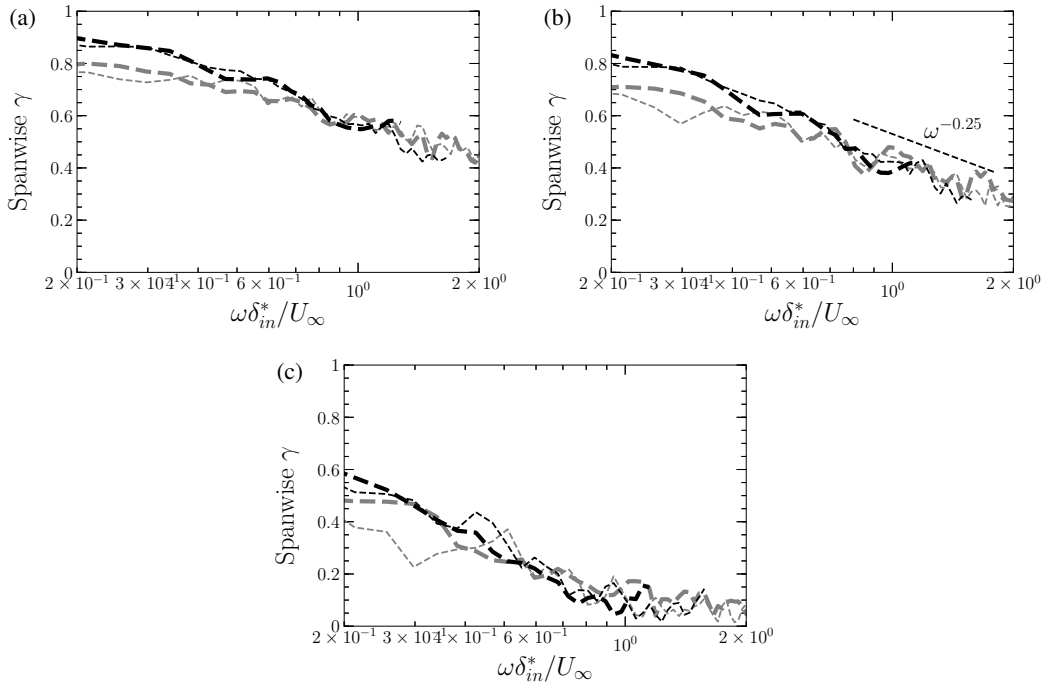


Figure 21: Spanwise $\gamma(\xi_z, \omega)$ frequency distribution for different spatial separations at four location on the aerofoil suction side: ZPG locations $x/c = -0.60$ (thin gray line) and $x/c = -0.47$ (thick gray line); APG locations $x/c = -0.14$ (thin black line), $x/c = -0.08$ (thick black line). (a) $\xi_z/c = 0.0019$; (b) $\xi_z/c = 0.0025$; (c) $\xi_z/c = 0.0049$.

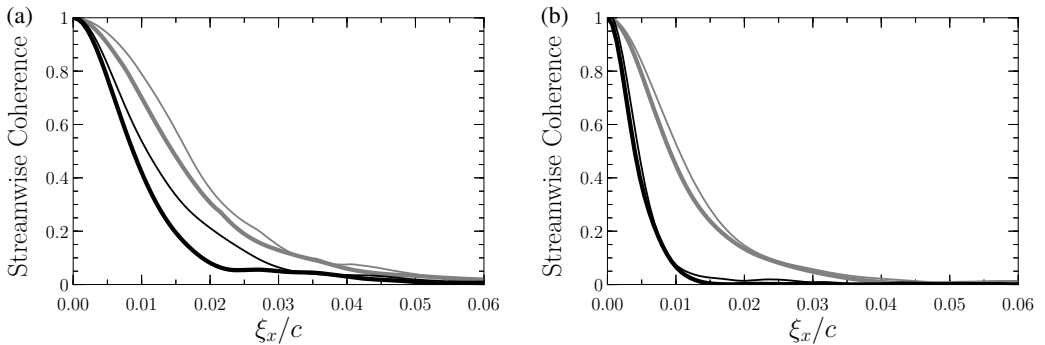


Figure 22: Coherence functions, γ^2 , at various streamwise separations on the aerofoil suction side: --, ZPG locations $x/c = -0.60$ (thin gray line) and $x/c = -0.47$ (thick gray line); --, APG locations $x/c = -0.14$ (thin black line), $x/c = -0.08$ (thick black line). (a) 1600 Hz (b) 5000 Hz.

671 All the above is also consistent with what has been previously observed for the main
 672 contributors to wall-pressure fluctuations in a turbulent boundary layer: on one hand, the wall-
 673 pressure behaviour at high frequencies is predominantly controlled by smaller structures in the
 674 inner layer, with short delay times and steep coherence decay rates with distance (Schloemer
 675 1967; Van Blitterswyk & Rocha 2017); on the other hand, the bigger outer-layer structures,
 676 characterized by longer decay lengths, dominate the wall-pressure coherence at low to mid

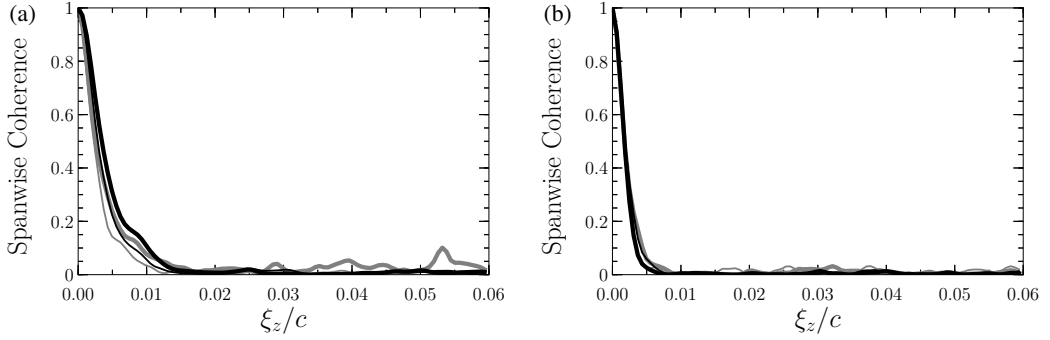


Figure 23: Coherence functions, γ^2 , at various spanwise separations on the aerofoil suction side: ZPG locations $x/c = -0.60$ (thin gray line) and $x/c = -0.47$ (thick gray line); APG locations $x/c = -0.14$ (thin black line), $x/c = -0.08$ (thick black line). (a) 1600 Hz and (b) 5000 Hz.

677 frequencies (Bull 1996; Palumbo 2012). The observed increase of spanwise coherence with
 678 APG in the low- to mid-frequency range can be related to the larger lifted turbulent structures
 679 seen in figure 11 (b).

680 In figures 24 and 25, the magnitude of the normalized longitudinal and lateral CSD
 681 are plotted versus the phase $\omega\xi_{x,z}/U_c$, with U_c the convective velocity, for several spatial
 682 separations for ZPG and APG cases. The streamwise $\gamma(\xi_x, \omega)$ and spanwise $\gamma(\xi_z, \omega)$
 683 measure the loss of coherence of the eddies as they move downstream and, similarly, the
 684 decrease of coherence of the eddies in the spanwise direction, respectively (Schloemer 1967).
 685 In figures 24 and 25, the dashed-dotted lines represent the curves found to fit the data of Corcos
 686 (1964) for ZPG TBL on a flat plate, $\exp(-\alpha_x \omega \xi_x / U_c)$ with $\alpha_x = 0.11$ and $\exp(-\alpha_z \omega \xi_z / U_c)$
 687 with $\alpha_z = 0.8$ and 0.714 . The convection velocities considered here correspond to about
 688 $U_c \approx 0.8U_\infty$ for ZPG flow and $U_c \approx 0.5U_\infty$ for APG flow, similarly to what was found by Na
 689 & Moin (1998), who observed a mean convection velocity of $U_c \approx 0.79U_\infty$ in ZPG flow and
 690 $U_c \approx 0.56U_\infty$ in APG flow, or by Schloemer (1967) who found a mean convection velocity
 691 of $U_c \approx 0.75U_\infty$ in ZPG flow and $U_c \approx 0.54U_\infty$ in APG flow. The decay rates α_x and α_z
 692 at the four locations analyzed here are obtained by fitting the data at different streamwise spatial
 693 separations and are plotted in the figures for each location using black solid lines. As shown
 694 in figure 24, the APG results display lower values of $\gamma(\xi_x, \omega)$ for a fixed $\omega\xi_x/U_c$ compared
 695 to the ZPG ones, which corresponds to an increase of α_x in the APG region. Indeed, a good
 696 fit to the data is found for the exponential decay of $\alpha_x = 0.11$ and $\alpha_x = 0.14$ for the ZPG
 697 locations, and $\alpha_x = 0.23$ and $\alpha_x = 0.29$ for the APG ones. For the present CD aerofoil, the
 698 ZPG coherence decays with the phase similarly (sensor 7) or more rapidly (sensor 9) than
 699 what was found by Corcos (1964). These trends in both ZPG and APG are consistent with
 700 the findings of Hu (2021), Brooks & Hodgson (1981) and Schloemer (1967). For instance,
 701 Hu (2021) reported $\alpha_x = 0.14$ in ZPG flow and $\alpha_x = 0.2$ in APG flow. In a flow with
 702 milder APG, Brooks & Hodgson (1981) observed a $\alpha_x = 0.19$. Given the difference in flow
 703 condition, this again suggests that the streamwise decay coefficient α_x hardly depends on
 704 the Reynolds number, consistently with the results of Sillero *et al.* (2014) and Pargal *et al.*
 705 (2022) on velocity correlations. In turn, this suggests that the empirical correlation of α_x
 706 with friction velocity or Reynolds number based on momentum thickness (equations (2) and
 707 (4) in Hu (2021)) may not apply at lower Re_θ . In figure 24, the curves for different streamwise
 708 separations tend to collapse for frequencies higher than a characteristic value, which varies
 709 with sensor location, decreasing as it moves downstream. The collapse implies a constant

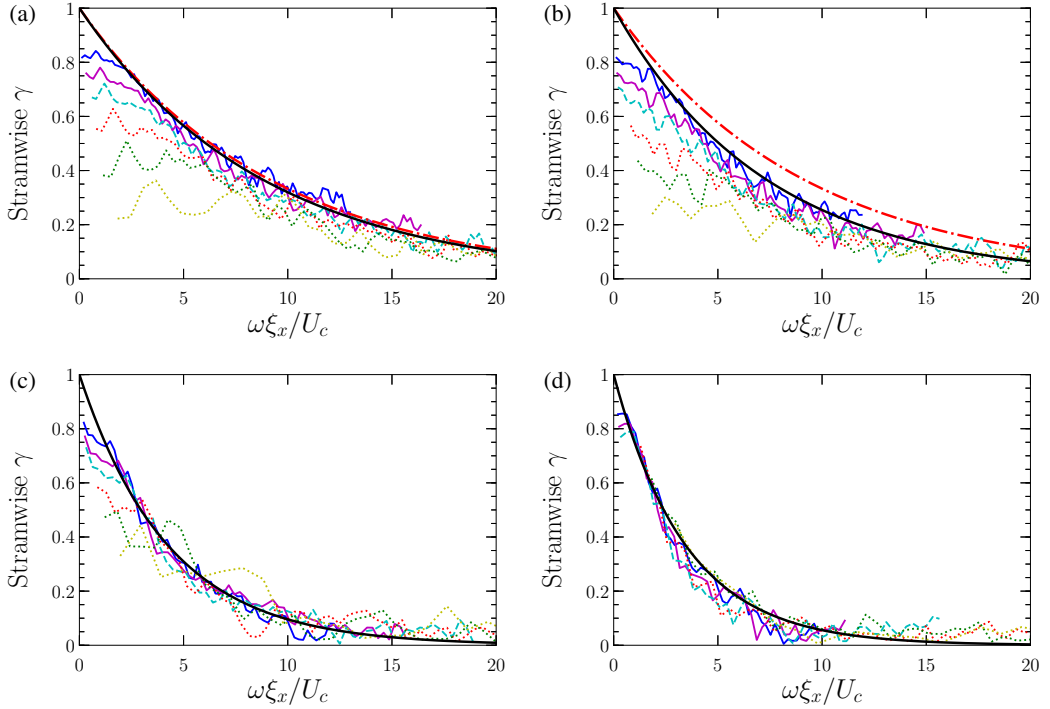


Figure 24: Streamwise $\gamma(\xi_x, \omega)$ versus the phase $\omega\xi_x/U_c$ for ZPG and APG positions. (a) $x/c = -0.60$; (b) $x/c = -0.47$; (c) $x/c = -0.14$; and (d) $x/c = -0.08$. — (blue), $\xi_x/c = 0.013$; - (purple), $\xi_x/c = 0.016$; -- (turquoise), $\xi_x/c = 0.021$; \cdots (red), $\xi_x/c = 0.026$; \cdots (green), $\xi_x/c = 0.037$; \cdots (olive), $\xi_x/c = 0.061$; - - - (red), $\exp(-0.11\omega\xi_x/U_c)$; -, $\exp(-\alpha_x\omega\xi_x/U_c)$ with $\alpha_x = 0.11$ for (a), $\alpha_x = 0.14$ for (b), $\alpha_x = 0.23$ for (c) and $\alpha_x = 0.29$ for (d).

710 decay rate of the wall-pressure fluctuations for the high-frequency range. These results are
 711 consistent with the comparisons seen in figures 18 to 22.

712 On the other hand, in figure 25, similar smaller changes in γ in the spanwise direction
 713 between ZPG and APG flows are found as observed by Schloemer (1967), Brooks & Hodgson
 714 (1981) and Hu (2021). In figure 25, a good fit to the data is found for the exponential decay
 715 with $\alpha_z = 0.76$ and $\alpha_z = 0.70$ for the two locations in the ZPG region respectively, and
 716 $\alpha_z = 0.48$ and $\alpha_z = 0.55$ for the APG ones, which yields a 36% variation in the spanwise
 717 direction compared to about a factor of two in the streamwise direction. For instance, Hu
 718 (2021) reported $\alpha_z = 0.75$ in ZPG and $\alpha_z = 0.5$ for the APG TBL in table 1, which yields a
 719 similar 33% variation in the spanwise direction. This in turn suggests that the spanwise decay
 720 coefficient α_z is weakly dependent on the Reynolds number, consistently with the results
 721 of Sillero *et al.* (2014) and Pargal *et al.* (2022) on velocity correlations. The variations of α_z
 722 in ZPG and APG flows are also consistent with data shown in figures 19 to 23. The observed
 723 similarity in the decay coefficient variations across a wide range of Reynolds numbers can
 724 help modelling the spatial coherence of wall pressure fluctuations, as an essential part of
 725 trailing edge noise prediction.

726 In the present compressible DNS case, the range of frequency considered is $0.069 \leq$
 727 $\omega\delta^*/U_\infty \leq 1.12$ to neglect the high-frequency acoustic contribution (i.e. additional noise
 728 source in the wake), which produces an increase of the spanwise $\gamma(\xi_z, \omega)$ and streamwise
 729 $\gamma(\xi_x, \omega)$ distributions as indicated in figure 25 (c) for $\xi_z/c = 0.0043$ (green dotted line).

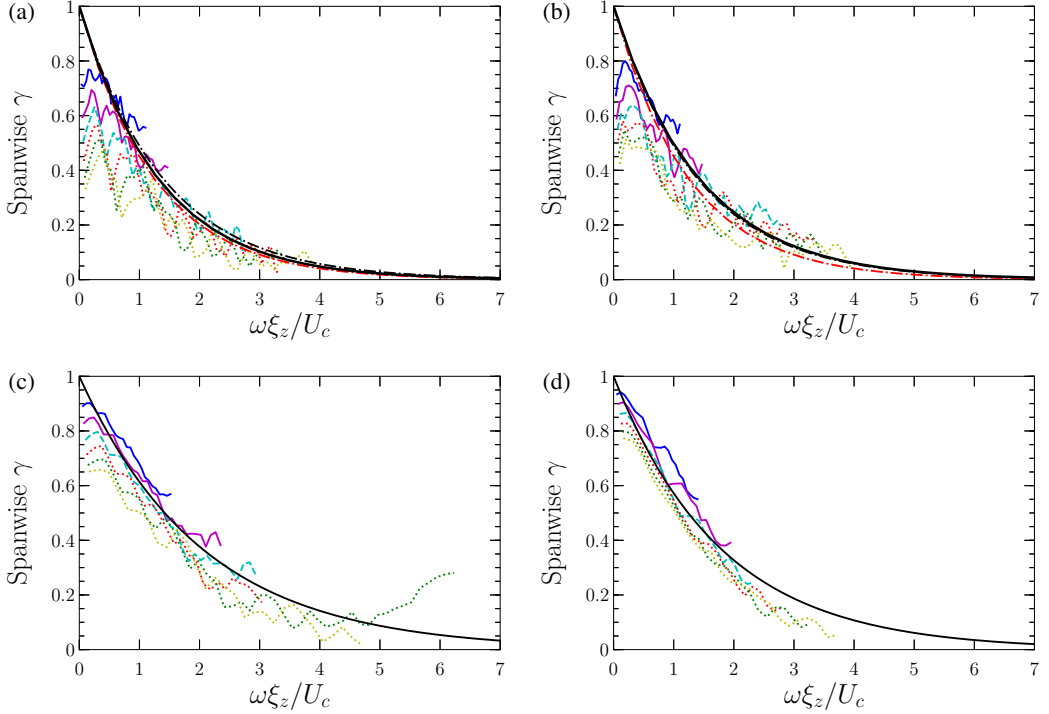


Figure 25: Spanwise $\gamma(\xi_z, \omega)$ versus the phase $\omega\xi_z/U_c$. (a) $x/c = -0.60$; (b) $x/c = -0.47$; (c) $x/c = -0.14$; and (d) $x/c = -0.08$. - (blue), $\xi_z/c = 0.0019$; - (purple), $\xi_z/c = 0.0025$; -- (turquoise), $\xi_z/c = 0.0031$; \cdots (red), $\xi_z/c = 0.0037$; \cdots (green), $\xi_z/c = 0.0043$; \cdots (olive), $\xi_z/c = 0.0056$; - - - $\exp(-0.714\omega\xi_z/U_c)$ and (red) $\exp(-0.8\omega\xi_z/U_c)$; -, $\exp(-\alpha_z\omega\xi_z/U_c)$ with $\alpha_z = 0.76$ for (a), $\alpha_z = 0.70$ for (b), $\alpha_z = 0.48$ for (c) and $\alpha_z = 0.55$ for (d).

730 Additionally, for a given pressure gradient, the decay rates are quite sensitive to a change in
 731 the convection velocity. Specifically, a lower U_c shifts $\gamma(\xi_{x,z}, \omega)$ towards higher $\omega\xi_{x,z}/U_c$,
 732 which gives a smaller decay rate.

733 A coherence length of wall-pressure fluctuations at each frequency can then be defined by
 734 the following expression in both streamwise and spanwise directions:

$$735 \quad L_{x,z}(f) = \int_0^{\infty} \gamma(\xi_{x,z}, f) d\xi_{x,z}. \quad (4.2)$$

736 The coherence length distributions in the same frequency range as above are plotted in
 737 figure 26 for the four positions on the CD aerofoil. Hu (2021)'s measurements over a more
 738 limited frequency range for the ZPG and APG flow conditions in table 1 are also shown.
 739 Despite the different Re_θ , the two sets of data show very similar results in the ZPG region for
 740 both coherence lengths. In the APG the trends are similar with smaller streamwise coherence
 741 length and larger spanwise one than in ZPG, but their roll-off occurs at a higher reduced
 742 frequency $\omega \delta^*/U_e$ closer to 1 (Reynolds number effect similar to what is observed for the PSD
 743 of the wall-pressure fluctuations). Consequently both L_z for ZPG and APG respectively merge
 744 almost a decade later in frequency in Hu (2021)'s data. The effect of APG on the coherence
 745 lengths is in fact consistent with what was found in Hu (2021) and Van Blitterswyk & Rocha
 746 (2017). The difference in the roll-off between APG and ZPG profiles, for both $L_x(f)$ and
 747 $L_z(f)$, reflects the effect of APG on the PSD spectra (see figure 12). At low frequencies, both

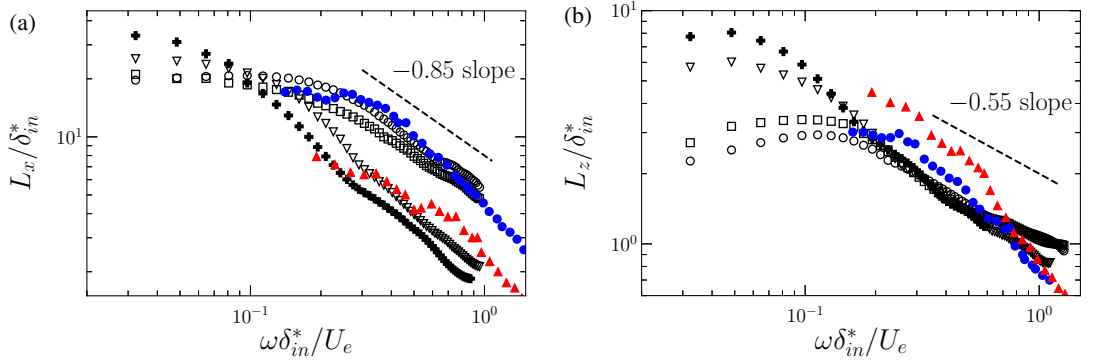


Figure 26: Normalized coherence lengths for ZPG locations (\circ , $x/c = -0.60$ and \square , $x/c = -0.47$) and APG locations (∇ , $x/c = -0.14$ and \blacktriangle , $x/c = -0.08$) in (a) streamwise and (b) spanwise directions. \bullet (blue) ZPG data by Hu (2021) at $Re_\theta = 4889$; \blacktriangle (red) APG data by Hu (2021) at $Re_\theta = 8670$.

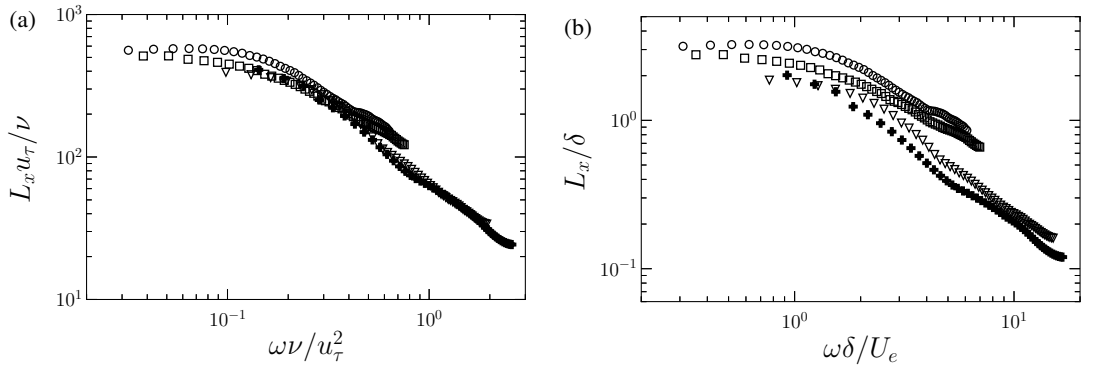


Figure 27: Normalized streamwise coherence lengths for ZPG locations (\circ , $x/c = -0.60$ and \square , $x/c = -0.47$) and APG locations (∇ , $x/c = -0.14$ and \blacktriangle , $x/c = -0.08$) in inner (a) and outer (b) variable scalings.

748 coherence lengths $L_{x,z}(f)$ increase with APG significantly. At middle to high frequencies,
 749 lower levels are found for the APG profiles compared with the ZPG ones, with a drop in the
 750 streamwise coherence length L_x much more marked than in the spanwise one L_z that stays
 751 almost similar at all locations. Indeed, as also observed by Van Blitterswyk & Rocha (2017)
 752 at a higher Re_θ , the intensity of smaller-scale structures with faster decay increases, as well
 753 as the size of large-scale structures.

754 Comparison between the streamwise correlation lengths normalized using inner (figure
 755 27 (a)) and outer (figure 27 (b)) variables shows that a better collapse at all four locations
 756 is obtained with an inner scaling. However, for the spanwise correlation length, a better collapse
 757 is obtained using the outer variables (figure 28 (b)) compared to figure 28 (a)).

758

4.3. Wavenumber-frequency spectra

759 The wavenumber-frequency spectral density of the wall-pressure fluctuations, $\Psi_{pp}(\mathbf{k}; \omega)$, is
 760 related to the CSD $\Psi_{pp}(\xi; \omega)$ by a 2D spatial Fourier transform (see section 2.1). In figures
 761 29 and 30, the normalized two-dimensional wavenumber-frequency spectra, $\bar{\Psi}_{pp}(\mathbf{k}; \omega) =$
 762 $\Psi_{pp}(\mathbf{k}; \omega)(U_\infty/\tau_w^2 \delta_{in}^3)$, is plotted in the normalized wavenumber domain $(k_x \delta_{in}^*, k_z \delta_{in}^*)$

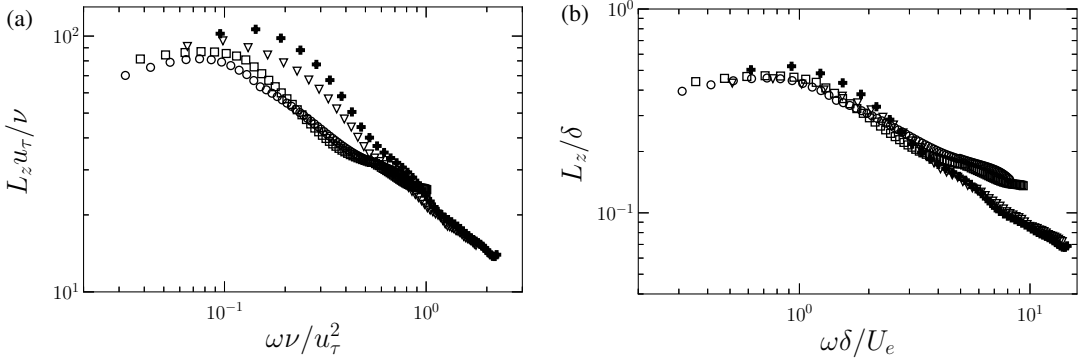


Figure 28: Normalized spanwise coherence lengths for ZPG locations (\circ , $x/c = -0.60$ and \square , $x/c = -0.47$) and APG locations (∇ , $x/c = -0.14$ and $+$, $x/c = -0.08$) in inner (a) and outer (b) variable scalings.

763 at three dimensionless frequency values, with k_x and k_z the streamwise and spanwise
 764 wavenumbers, respectively. Note that the same dimensionless frequencies are used for the
 765 four locations: a low frequency $\omega \delta_{in}^* / U_\infty = 0.34$, a middle frequency $\omega \delta_{in}^* / U_\infty = 0.76$,
 766 and a high frequency $\omega \delta_{in}^* / U_\infty = 1.73$. At the low frequency, the convective contribution
 767 centred around the convective wavenumber $k_x = k_c$ (with $k_c = \omega / U_c$) is predominant. On
 768 the other hand, the acoustic contribution centred around the acoustic wavenumber $k_x = k_0$
 769 is not visible. At the high frequency $\omega \delta_{in}^* / U_\infty = 1.73$, however, the acoustic contribution
 770 appears and separates from the convective one, as seen in figure 30. The trace of the acoustic
 771 domain matches an ellipse with its centre at $(k_0 M / \beta^2, 0)$, a major radius of k_0 / β^2 , and a
 772 minor radius of k_0 / β with the Prandtl-Glauert factor given by $\beta = \sqrt{1 - M^2}$ (see dashed red
 773 lines in figures 29 and 30), as also found in the compressible LES of Cohen & Gloerfelt
 774 (2018). At the low frequency, the red ellipse merges with the convective domain, while at the
 775 higher frequencies it is clearly visible. As noted by Cohen & Gloerfelt (2018), it is rare to
 776 capture the acoustic contribution and this is a first case in such a non-equilibrium turbulent
 777 boundary layer with high APG. At higher frequencies (≈ 10 kHz for APG locations as seen
 778 in figure 30), the acoustic contribution to the fluctuations becomes significant. Indeed, for
 779 higher frequencies, darker contours around the acoustic wavenumber and lighter contours in
 780 the convective region are seen in figures 29 and 30. The convective contribution seen in the
 781 figures has an antisymmetric distribution along k_x and an elongated elliptical shape with a
 782 major axis in the k_z direction. The convective ridge in k_x in the ZPG spectra in figure 29
 783 is slightly smaller (with higher U_c) than in the APG spectra in figure 30. This behaviour
 784 is consistent with what was found by Cohen & Gloerfelt (2018), Salze *et al.* (2015) and
 785 Bull (1996). Thus, as seen before the wall-pressure field is more coherent in the streamwise
 786 direction for the ZPG region than for the APG one (see section 4.2).

787 In figure 31, the normalized wavenumber-frequency spectra for the four locations are also
 788 plotted as functions of frequency for increasing $k_x \delta_{in}^*$ in the range $0.36 \leq k_x \delta_{in}^* \leq 2.11$,
 789 with increments of 0.25 going from top (solid black line) to the bottom (solid thick gray
 790 line) of the plot. The maximum of each spectrum in figure 31 corresponds to the primary
 791 convective peak. For higher $k_x \delta_{in}^*$ (i.e. solid thick gray line with $k_x \delta_{in}^* = 2.11$ in figure
 792 31), the primary convective peak moves to higher frequencies (Bull 1996; Choi & Moin
 793 1990). In the same way, as indicated in the contour plots of figures 29 and 30, as the
 794 frequency increases the convective ridge moves to higher wavenumbers. This behaviour can
 795 be analyzed more in detail if considering, for example, figure 29 (a) for $x/c = -0.60$; in this

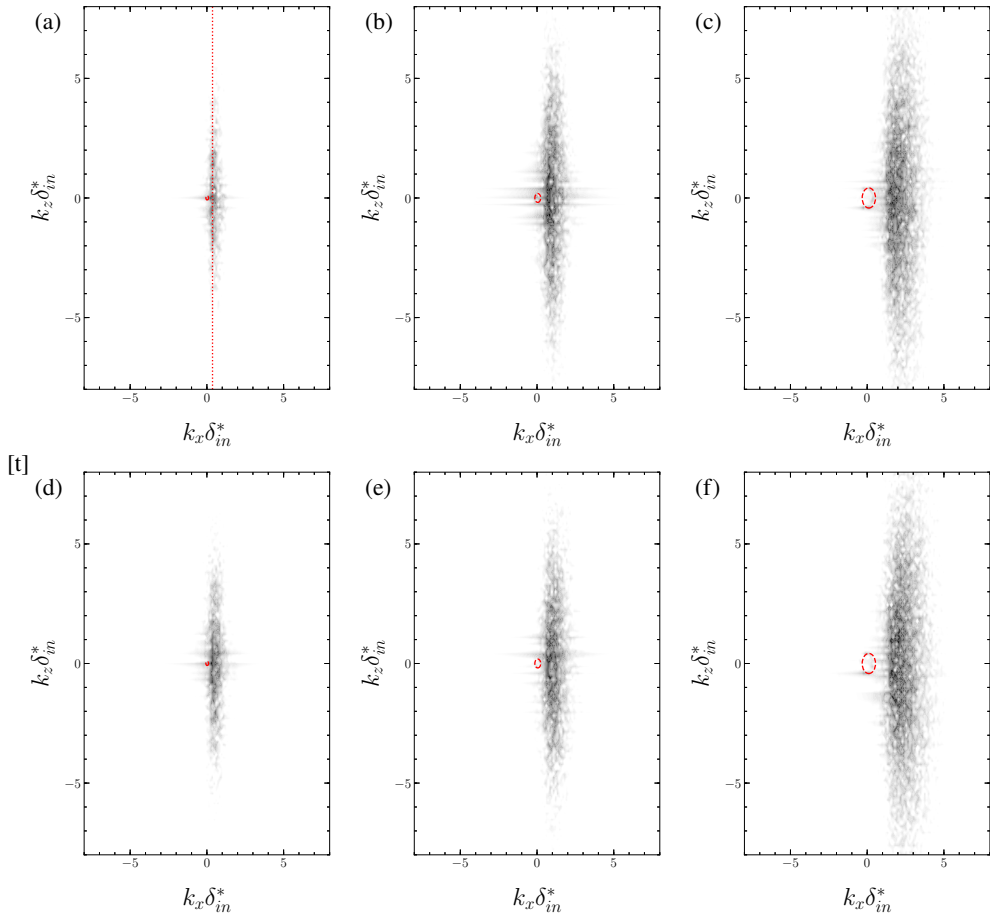


Figure 29: Normalized two-dimensional wavenumber-frequency spectra $\overline{\Psi}_{pp}(\mathbf{k}; \omega) = \Psi_{pp}(\mathbf{k}; \omega)(U_\infty/\tau_w^2 \delta_{in}^{*3})$ measured at three dimensionless frequencies: left column $\omega\delta_{in}^*/U_\infty = 0.34$; center column $\omega\delta_{in}^*/U_\infty = 0.76$; right column $\omega\delta_{in}^*/U_\infty = 1.73$. ZPG locations: (a), (b), (c) $x/c = -0.60$; (d), (e), (f) $x/c = -0.47$. Trace of the acoustic domain (red dashed line) (Cohen & Gloerfelt 2018) and centre of the convective ridge (red dotted line).

796 case, the convective ridge is centred around $k_x\delta_{in}^* = 0.36$ for $\omega\delta_{in}^*/U_\infty = 0.34$. Thus, at this
 797 normalized frequency, in figure 31 (a), a maximum is seen for the solid black curve which
 798 corresponds to $k_x\delta_{in}^* = 0.36$ (see red dotted line in figures 29 (a) and 31 (a)). For APG, the
 799 acoustic peak is also seen at higher frequencies. If considering, for example, figure 29 (f),
 800 for $x/c = -0.08$, the acoustic domain is centred around $k_x\delta_{in}^* = 0.40$ for $\omega\delta_{in}^*/U_\infty = 1.73$.
 801 Thus, around this frequency in figure 31 (d), a maximum is seen for the solid black curve
 802 which corresponds to a closer $k_x\delta_{in}^*$ of 0.36. The result shows that the high-frequency humps
 803 observed in wall pressure PSD in a non-equilibrium flow such as the present one is due to
 804 acoustic contribution. Therefore, it may not be appropriate to model high-frequency humps
 805 of this kind directly based on aerodynamic boundary layer parameters (e.g. by Dominique
 806 *et al.* 2022).

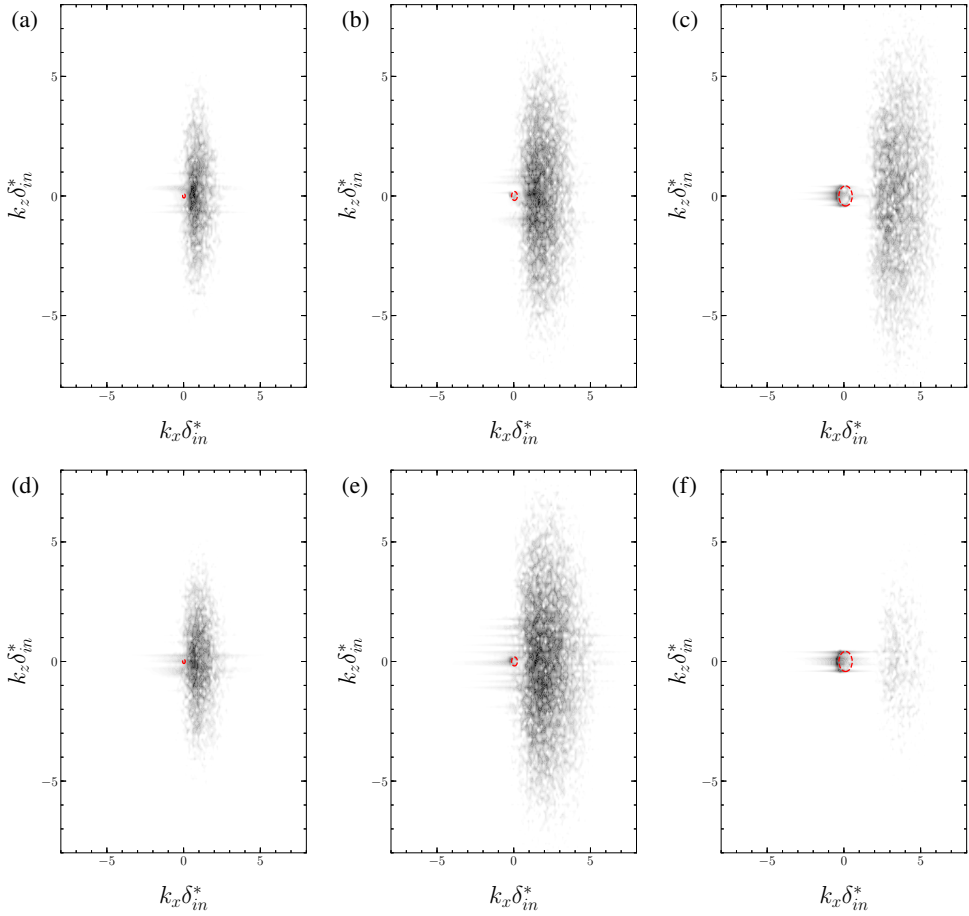


Figure 30: Normalized two-dimensional wavenumber-frequency spectra $\overline{\Psi}_{pp}(\mathbf{k}; \omega) = \Psi_{pp}(\mathbf{k}; \omega)(U_\infty / \tau_w^2 \delta_{in}^{*3})$ measured at three dimensionless frequencies: left column $\omega \delta_{in}^* / U_\infty = 0.34$; center column $\omega \delta_{in}^* / U_\infty = 0.76$; right column $\omega \delta_{in}^* / U_\infty = 1.73$. APG locations: (a), (b), (c) $x/c = -0.14$; (d), (e), (f) $x/c = -0.08$. Trace of the acoustic domain (red dashed line) (Cohen & Gloerfelt 2018).

807

4.4. Convection velocity

808 In this section, the convection velocity U_c is calculated from the DNS database for the four
 809 locations under analysis. Generally speaking, the convection velocity of a Fourier mode is
 810 expressed as $U_c = \omega / k_x = f \lambda_x$. However, for a given frequency a spectrum of wavenumber
 811 is found, and vice-versa, as seen in figures 29, 30 and 31 (Del Álamo & Jiménez 2009). In
 812 general, Taylor's frozen turbulent approximation (Taylor 1938) that assumes a uniform U_c
 813 equal to the local mean velocity is commonly used. Such an approximation, acceptable for
 814 low frequencies and low wavenumbers, neglects the dependence of U_c on eddy size leading
 815 to errors in the interpretation of large-scale structures in jets for instance (Del Álamo &
 816 Jiménez 2009). To overcome this limitation, different definitions of U_c have been proposed,
 817 which consider its dependence on wavenumber, frequency and spatial separation (Wills 1964;
 818 Hussain & Clark 1981; Goldschmidt *et al.* 1981).

819 In the following section, the convection velocities as functions of frequency, wavenumber
 820 or spatial separation are calculated for ZPG and APG TBLs on the CD aerofoil and compared

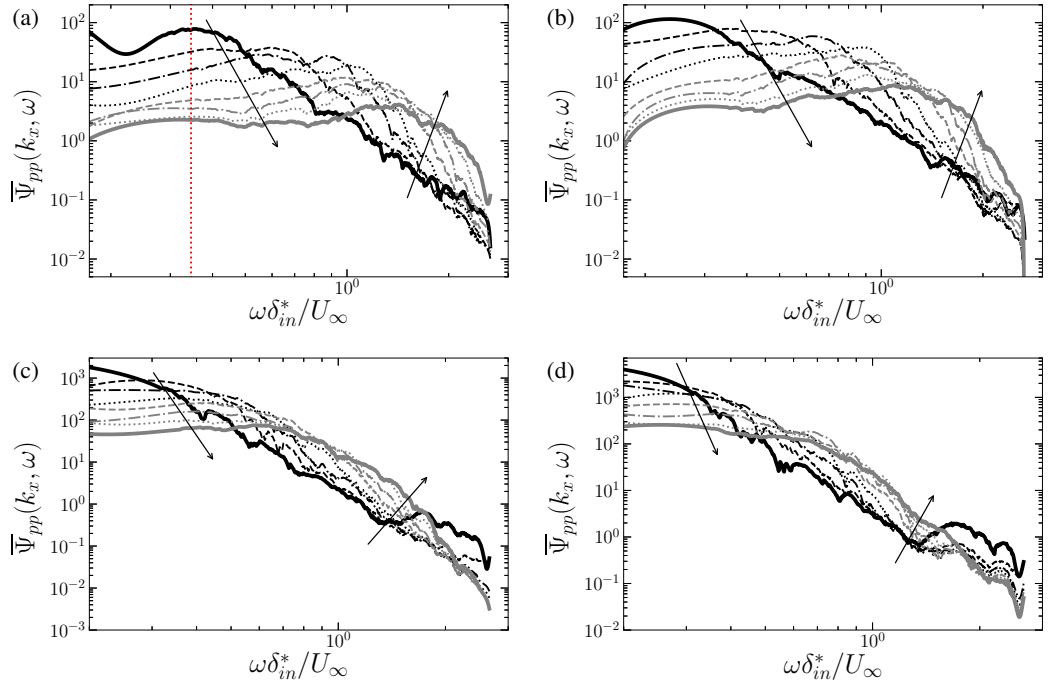


Figure 31: Normalized two-dimensional wavenumber-frequency spectra as function of frequency at increasing $k_x \delta_{in}^*$. $k_x \delta_{in}^* = 0.36$ (solid black line) to $k_x \delta_{in}^* = 2.11$ (solid thick gray line), with increments of 0.25. (a) $x/c = -0.60$; (b) $x/c = -0.47$; (c) $x/c = -0.14$; and (d) $x/c = -0.08$.

821 with available data by Choi & Moin (1990), Na & Moin (1998), Cohen & Gloerfelt (2018)
 822 and Burton (1973).

823 4.4.1. Convection velocity as a function of frequency

824 The convection velocity $U_c(\omega)$ is extracted from a linear interpolation of the phase $\omega \xi_x / U_c$
 825 in the cross-spectrum, $\Psi_{pp}(\xi; \omega)$, and scaled with inner and outer boundary layer variables,
 826 as shown in figure 32. The range of spatial separations ξ_x for which the phase is linear within
 827 about 10% is considered for the extraction of $U_c(\omega)$.

828 The inner variables scaling shown in figure 32 (a) shows a good collapse of the spectra.
 829 Generally, the convection velocity increases with frequency, reaching a maximum and then
 830 slightly decreases with frequency, as the size of structures in the boundary layer, proportional
 831 to the wavelength, decreases (Schloemer 1967). For a given value of $\omega \delta / u_\tau$, the ratio
 832 $U_c(\omega) / U_\infty$ is lower for APG than for ZPG, because the smallest turbulent structures located
 833 near the wall are subjected to a slower flow, and the largest ones lifted from the wall
 834 mostly convect with the bulk velocity that is also lower (see figure 11). Therefore, smaller
 835 mean convection velocities of the turbulent eddies are found. In figure 32, as the frequency
 836 increases, $U_c(\omega) / U_\infty$ reaches approximately 0.8 for the ZPG cases and 0.5 for the APG
 837 ones, as previously found by Bull (1996) and used in section 4.2. Moreover, in APG the high-
 838 frequency limit slightly decreases. On the other hand, for ZPG the ratio $U_c(\omega) / U_\infty$ increases
 839 to a maximum asymptotic value. The ratio found for the ZPG regions, at sensor 9 noticeably,
 840 is in good agreement with Choi's ZPG data (Choi & Moin 1990). At lower frequencies,
 841 the ratio decreases. This behaviour, also seen in Choi's ZPG data, is linked to the loss of

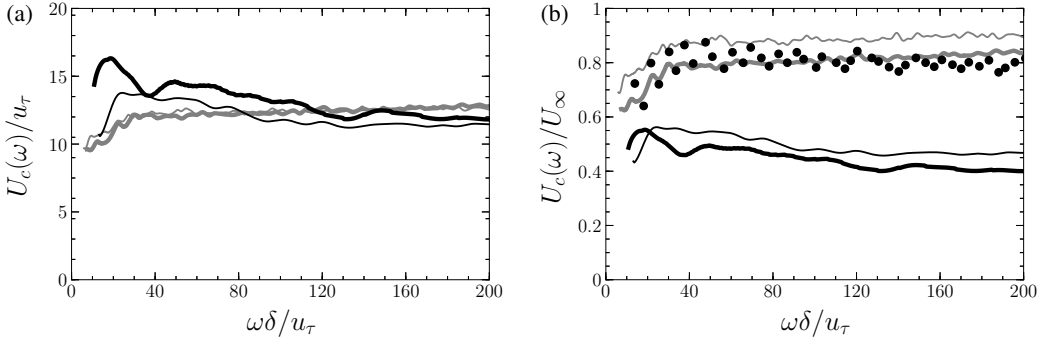


Figure 32: Normalized convection velocities as function of dimensionless frequency at four locations on the aerofoil suction side: ZPG locations $x/c = -0.60$ (thin gray line) and $x/c = -0.47$ (thick gray line); APG locations $x/c = -0.14$ (thin black line), $x/c = -0.08$ (thick black line). •, data by Choi & Moin (1990). (a) Inner variables scaling; (b) Outer variables scaling.

842 coherence of the turbulent structures seen in section 4.2 (figure 24). The convection velocity
 843 is slightly higher at sensor 7 most likely because of the history effect of the upstream FPG
 844 region (figure 15 (c) in Schloemer (1967)). The mean convection velocities calculated from
 845 these distributions are $U_c \approx 0.87 U_\infty$ for sensor 7, $U_c \approx 0.80 U_\infty$ for sensor 9, $U_c \approx 0.50 U_\infty$
 846 for sensor 21 and $U_c \approx 0.44 U_\infty$ for sensor 24. In turn, these ratios correspond to coherence
 847 decay rates $\alpha_x = 0.13$ and $\alpha_z = 0.82$ at sensor 7, and $\alpha_x = 0.25$ and $\alpha_z = 0.49$ at sensor 24,
 848 while at sensors 9 and 21 the coherence decay rates are as indicated in figures 24 and 25.

849 Overall, figure 32 shows uniform distributions for $U_c(\omega)$, consistent with previous
 850 measurements in both ZPG (see for instance figure 15 (a) in Schloemer (1967)) and APG
 851 flows (see for instance figure 15 (b) in Schloemer (1967); figure 19 in Brooks & Hodgson
 852 (1981)). The results also indicate that the convection velocity scales well with friction velocity
 853 for the majority of the frequency range, even in highly non-equilibrium flows. The differences
 854 observed at sensor 24 at low frequencies could be due to the vicinity of this location to the
 855 trailing edge (Wu *et al.* 2020; Messiter 1970). Note also that the data presented do not extend
 856 to lower frequencies where the ratio may be sensitive to the sampling period.

857 4.4.2. Convection velocity as a function of streamwise wavenumber

858 The convection velocity can be defined from the wavenumber-frequency spectra, $\Psi_{pp}(k_x, \omega)$,
 859 as function of the streamwise wavenumber by considering the maximum of the frequency
 860 spectrum at a given wavenumber $[\partial \Psi_{pp}(k_x, \omega) / \partial \omega]_{\omega=\omega_c(k_x)} = 0$. Such a maximum
 861 corresponds to the convective frequency that gives $U_c(k_x) = -\omega_c(k_x) / k_x$. This scheme
 862 was proposed by Wills (1964) to consider the dependence of U_c on both wavenumber
 863 and frequency, overcoming the artifact of Taylor's approximation that is most likely not
 864 verified in the present highly sheared strongly non-equilibrium TBL (Moin 2009). Similarly,
 865 $U_c(k_x)$ can be defined considering the maximum of the wavenumber spectrum at a given
 866 frequency (Comte-Bellot & Corrsin 1971). The normalized convection velocities as functions
 867 of dimensionless streamwise wavenumber at the four locations on the aerofoil suction side
 868 are plotted in figure 33.

869 Inner and outer variable scaling are obtained using u_τ and U_∞ , respectively. The results
 870 are then compared with data by Choi & Moin (1990) and Panton & Linebarger (1974)'s
 871 model. In figures 33 (a) and 33 (b), a good agreement is found for the ZPG distributions with
 872 Choi & Moin (1990), and in the low to mid wavenumber range ($k_x \delta$ below 20) with Panton

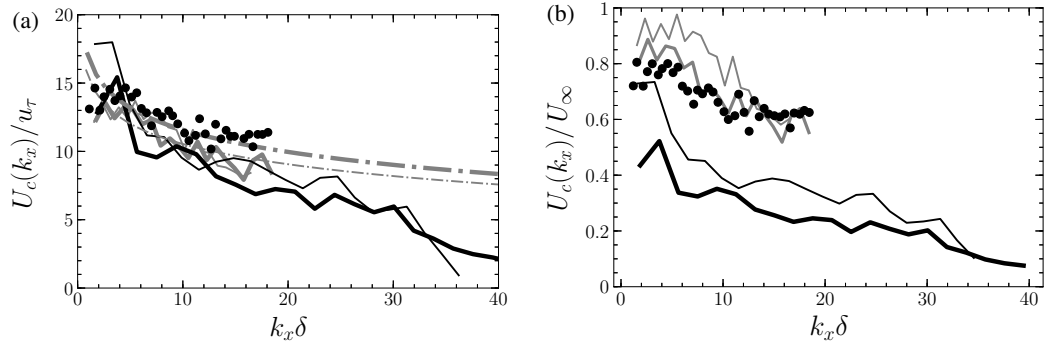


Figure 33: Normalized convection velocities as function of dimensionless streamwise wavenumber at four locations on the aerofoil suction side: ZPG locations $x/c = -0.60$ (thin gray line) and $x/c = -0.47$ (thick gray line); APG locations $x/c = -0.14$ (thin black line), $x/c = -0.08$ (thick black line). •, data by Choi & Moin (1990) and - · -, Panton & Linebarger (1974)'s model for $Re_\tau = 178$ and $Re_\tau = 185$, corresponding to sensors 7 (thin gray line) and 9 (thick gray line), respectively. (a) Inner variables scaling; (b) Outer variables scaling.

873 & Linebarger (1974)'s model (see both dashed dotted lines). Indeed, according to Panton &
 874 Linebarger (1974), a convective velocity overlap law, similar to the friction mean velocity
 875 log-law, can be defined in the mid wavenumber range, in which large and small structures
 876 are both important. This overlap law depending upon the friction Reynolds number is plotted
 877 here for $Re_\tau = 178$ and $Re_\tau = 185$ corresponding to sensors 7 and 9 respectively (see
 878 table 1). The inner variable scaling of figure 33 (a) shows a good collapse of the spectra
 879 upon $k_x \approx 15/\delta$, with APG levels of the same order of the ZPG ones. In figure 33 (b), for
 880 small scale structures (or high k_x), the ratio U_c/U_∞ is around 0.6 for ZPG. It decreases in
 881 the APG region to 0.2 and 0.1 at sensors 21 and 24 respectively. For large scale structures
 882 (or low k_x), the ratio U_c/U_∞ is higher around 0.8 for ZPG. It again decreases in the APG
 883 region to 0.7 and 0.5 at sensors 21 and 24 respectively. Due to the difficulty in extracting the
 884 maxima of the wavenumber-frequency spectra in a discrete frequency range, the distributions
 885 of convective velocities in figure 33 are quite scattered particularly at low wavenumbers (or at
 886 the lowest frequencies), which corresponds to the noisiest part of the spectra. Nevertheless,
 887 at lower k_x , the convection velocities can be seen to slightly decrease, probably because for
 888 those wavenumbers the contribution of the outer region of the boundary layer is lower and
 889 the middle region contribution picks up.

890 As already observed by Choi & Moin (1990), at high frequencies and wavenumbers, a
 891 discrepancy between $U_c(\omega)$ and $U_c(k_x)$ is seen: $U_c(\omega) \approx 0.8U_\infty$ and $U_c(k_x) \approx 0.6U_\infty$
 892 for ZPG; and, $U_c(\omega) \approx 0.5U_\infty$ and $U_c(k_x) \approx 0.2U_\infty$ for APG. This is probably due to the
 893 $\Psi_{pp}(\mathbf{k}; \omega)$ characterized by a higher aspect ratio at high frequencies and wavenumbers, as
 894 also shown in figure 9 in Choi & Moin (1990), (see section 4.3 and Wu *et al.* (2019)). Overall,
 895 as discussed for $U_c(\omega)$, as k_x increases, the decrease of $U_c(k_x)$ is more evident for APG
 896 than for ZPG, probably due to the smaller (Lee & Sung 2008) and slower-moving eddies
 897 near the wall in an APG flow.

898 4.4.3. Convection velocity as a function of longitudinal separation

899 The convection velocity is also commonly defined from the cross-correlation $R_{pp}(\xi_x, \tau)$
 900 as function of the streamwise separation as $U_c(\xi_x) = \xi_x/\tau_{max}(\xi_x)$ where the time delay
 901 τ_{max} is given by the maximum $[\partial R(\xi_x, \tau)/\partial \tau]_{\tau=\tau_{max}(\xi_x)} = 0$. In figure 34, the normalized

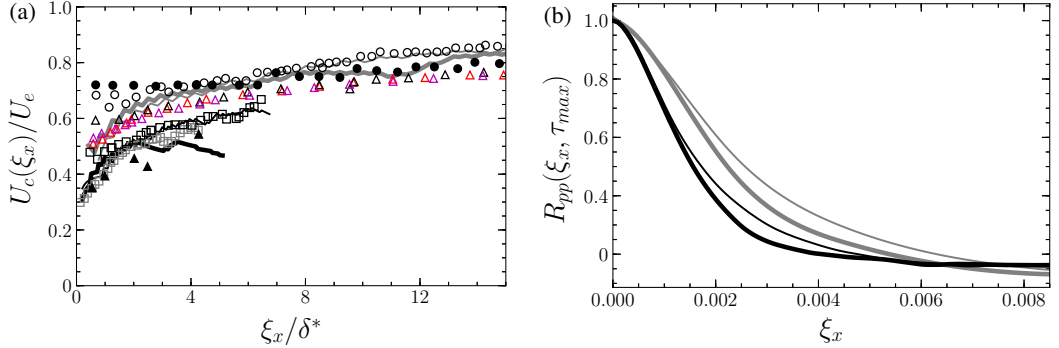


Figure 34: (a) Normalized convection velocities as function of longitudinal separation and (b) peaks of the longitudinal space-time correlation at four locations on the aerofoil suction side: ZPG locations $x/c = -0.60$ (thin gray line) and $x/c = -0.47$ (thick gray line); APG locations $x/c = -0.14$ (thin black line), $x/c = -0.08$ (thick black line). ●, data by Choi & Moin (1990); ○, ZPG data $x = 0.5$, and □, APG data $x = 0.85$ for attached TBL and separated TBL (grey) at $x/\delta_{in}^* = 120$ by Na & Moin (1998); △, ZPG (black), APGs (red), APGw (magenta) data by Cohen & Gloerfelt (2018); ▲, Burton (1973) APG's data.

902 convection velocities as function of longitudinal separation ξ_x/δ^* are shown, together with
 903 the peaks of the longitudinal space-time correlation at the four locations on the aerofoil
 904 suction side.

905 In figure 34 (a), the ratio $U_c(\xi_x)/U_e$ is seen to increase almost monotonously for all data
 906 sets as the longitudinal separation increases. In fact, as a group of turbulent eddies travel
 907 downstream, the smaller eddies die out more rapidly and the larger ones (with higher U_c
 908 and a longer life time) dominate the wall-pressure correlation, as evidenced in figure 34 (b).
 909 Indeed, as seen in figure 17, the time delay corresponding to the peaks of the longitudinal
 910 space-time correlation for a particular eddy is shorter in ZPG than in APG, so lower values
 911 of correlation and longer delay times are found in the APG flow. The relationship between
 912 APG and ZPG flows is similar to what it is found for $U_c(\omega)$ and $U_c(\xi_x)$. For a given value of
 913 ξ_x/δ^* the convective velocity is lower for APG than for ZPG (Na & Moin 1998; Schloemer
 914 1967). In figure 34 (a), the convection velocities at large separations ξ_x are close to what
 915 is found at low k_x : about $0.7U_e$ at $\xi_x = 11\delta^*$ (or $0.85U_\infty$) for ZPG and about $0.5U_e$ at
 916 $\xi_x = 5\delta^*$ (or about $0.55U_\infty$) for APG. On the other side, the convection velocities at small
 917 ξ_x separations are close to what is found at high k_x (see 33 (b)). A good agreement with
 918 the reference data is found for both APG and ZPG (Choi & Moin 1990; Na & Moin 1998;
 919 Cohen & Gloerfelt 2018; Burton 1973). This is also consistent with the APG region on
 920 the NACA0012 aerofoil as shown in figure 21 in Brooks & Hodgson (1981). Figure 34
 921 shows how an increase of Reynolds number is characterized by a faster decay in ξ_x with the
 922 low-frequency wall-pressure fluctuations retained for extended streamwise distances. This
 923 is a characteristic of hairpin structures (Van Blitterswyk & Rocha 2017), or long coherent
 924 motions containing a large number of smaller events.

925 In summary, for all three definitions of the convection velocity in the present highly non-
 926 equilibrium turbulent flow, the APG is seen to significantly reduce the convection velocity
 927 (by a factor 2 to 3), consistently with previously measured ZPG and APG TBL. In terms of
 928 scaling, good collapse is found when all defined convection velocity are normalized by the
 929 friction velocity u_τ .

930 5. Conclusions and discussion

931 In the present study, recent DNS results are used to examine statistics of flows under mean
 932 ZPG and APG at low free-stream Mach number on a curved surface on which grows a highly
 933 non-equilibrium turbulent boundary layer. The DNS database has been previously obtained
 934 from a 3D compressible DNS of the flow over a CD aerofoil by Wu *et al.* (2018), which
 935 has been developed in order to reproduce the experimental set-up performed in the anechoic
 936 open jet wind-tunnel of the Université de Sherbrooke (Padois *et al.* 2015; Jaiswal 2020).
 937 Single point turbulent statistics and higher order statistics for wall-pressure fluctuations are
 938 investigated at four locations on the aerofoil corresponding to increasing $Re_\theta = 319, 390,$
 939 877 and 1036 , as well as $Re_\tau = 178, 185, 210$ and 203 . Those locations correspond to ZPG
 940 (sensors 7 and 9) and APG (sensors 21 and 24) locations on the suction side of the CD
 941 aerofoil, respectively.

942 The turbulence statistics show that the strong APG has a significant effect on the mean
 943 velocity profiles and velocity fluctuations, as well as on wall-pressure statistics (PSD
 944 distributions, two-point correlations, coherence and wavenumber-frequency spectral density
 945 of wall-pressure fluctuations). This effect is more prominent on the outer region of the
 946 boundary layer. Single point turbulent velocity statistics and mean-flow distributions are in
 947 agreement with available literature data by Spalart (1988), Abe *et al.* (2005), Schlatter &
 948 Örlü (2010), Vinuesa *et al.* (2017), Watmuff (1989) and Smits *et al.* (1983) for instance. On
 949 the one hand, the boundary layer thicknesses (δ , δ^* and θ), as well as the shape factor (H),
 950 increase moving downstream from ZPG to APG. Even though the transition to turbulence
 951 is triggered by a LSB at the leading edge, the boundary-layer state at mid-chord for sensors
 952 7 and 9 are close to a fully turbulent flat-plate boundary layer. Further downstream, the
 953 airfoil camber triggers a strong variation of mean pressure gradients shown by the Clauser
 954 parameter β_c , indicating the non-equilibrium state of the turbulent boundary layer near the
 955 trailing edge. On the other hand, the skin friction coefficient C_f decreases slowly in the ZPG
 956 region and much faster towards the TE at increasing Reynolds numbers based on momentum
 957 thickness because of the strong APG. The scaling of C_f proposed by Volino (2020) partially
 958 holds but with a larger correction factor most likely caused by the present stronger APG.
 959 Moreover, the self-similarity of velocity fluctuations in the outer region of the boundary
 960 layer provided by the Zagarola-Smits scaling is also verified in the present strong non-
 961 equilibrium TBL. Particular attention has then been given for the first time to the effect of
 962 APG and of increasing Reynolds numbers on all higher order wall-pressure statistics that are
 963 necessary parameters in physically-based trailing-edge noise model as proposed by Amiet
 964 (1976) and Roger & Moreau (2005). The present wall-pressure data compare well with both
 965 measurements of Jaiswal (2020) and numerical results of Choi & Moin (1990), Na & Moin
 966 (1998), Spalart (1988), Abe *et al.* (2005) and Cohen & Gloerfelt (2018) for instance. All
 967 wall-pressure spectra exhibit a high-frequency range with a -5 slope attributed to the buffer
 968 layer. The mid-frequency range shows a -1 slope, the width of which slightly increases with
 969 the Reynolds number. It indicates more prominent contribution from the logarithmic layer
 970 to wall-pressure fluctuations. The spectra in the APG region exhibit higher levels at low to
 971 mid-frequency and a faster roll-off at high frequencies, a sign of transfer of energy from high
 972 to low frequencies consistent with the change of near-wall eddies in the TBL. As previously
 973 observed, the scalings of wall-pressure spectrum with outer and inner variables to collapse
 974 the low- and high-frequency range, respectively, applies in the ZPG region only, and not in
 975 the APG one. For the current strong APG flow, the best scaling variables are found to be U_e , δ
 976 and the wall-pressure r.m.s. (p_{rms}), or equivalently U_{ZS} , δ^* and p_{rms} . This suggests that the
 977 Zagarola-Smits velocity might be a relevant velocity scale for all attached TBLs. Moreover,
 978 this also stresses that, in a strong non-equilibrium turbulent boundary layer typical of low-

979 speed rotating machines as shown here, the overall wall-pressure fluctuations are dominated
 980 by the large turbulent scales, the contribution of which increases with APG. [This also shows](#)
 981 [that the usual friction velocity considered in all previous analytical models of wall-pressure](#)
 982 [spectra is not the proper velocity scale in a flow with strong APG.](#) An alternative pressure
 983 scale is also found to be the local maximum Reynolds shear stress magnitude, the ratio of
 984 which with p_{rms} remains almost constant for the whole range of Reynolds number considered
 985 here, as also found previously by Na & Moin (1998) and Abe (2017) for instance.

986 Considering second-order statistics, normalized longitudinal and lateral CSD of wall-
 987 pressure fluctuations yield consistent results with previous measurements from Schloemer
 988 (1967), Brooks & Hodgson (1981) and Hu (2021). Streamwise cross-correlations are seen to
 989 decay rapidly with increasing longitudinal separation when moving downstream, indicating
 990 shorter coherence in the APG region than in the ZPG one. On the other hand, the decay of
 991 spanwise coherence with lateral separation is much slower. Moreover, the [spanwise](#) coherence
 992 decays faster with distance than the [streamwise](#) one in both ZPG and APG regions for all
 993 considered frequencies. Both streamwise and spanwise decay coefficients are also found to
 994 be quite insensitive to Reynolds numbers based on momentum thickness (at least over a
 995 decade), consistently with the results of Sillero *et al.* (2014) and Pargal *et al.* (2022) on
 996 velocity correlations. Streamwise and spanwise correlations lengths can then be defined
 997 and compared: in APG, smaller streamwise coherence length and larger spanwise one are
 998 obtained than in ZPG. Consistently with the trend observed on wall-pressure spectra, APG
 999 coherence lengths are larger at low frequencies and decay faster at high frequencies. [When](#)
 1000 [scaled with the outer variables \(boundary-layer displacement thickness and Zaragola-Smits](#)
 1001 [velocity\) the spanwise coherence lengths—the second key parameter to trailing-edge noise](#)
 1002 [predictions—are seen to better collapse at low and mid frequencies for all positions \(both](#)
 1003 [ZPG and APG\).](#) On the other hand, the streamwise coherence lengths are found to better
 1004 [scale with inner variables at all locations on the aerofoil suction side.](#)

1005 Finally, three different ways of defining the convection velocity in the present highly
 1006 non-equilibrium turbulent flow have been studied to investigate its dependence on frequency,
 1007 wavenumber and spatial separation. The results compare favorably with the numerical data of
 1008 Choi & Moin (1990), Na & Moin (1998) and Cohen & Gloerfelt (2018), and Burton (1973)'s
 1009 measurements. In the APG region, the convection velocities increase with longitudinal
 1010 separation and decrease with increasing frequency and wavenumber, whereas in the ZPG
 1011 region an asymptotic value is found for large separations and frequencies in agreement with
 1012 previous observation of ZPG TBLs. Moreover, compared to the free-stream velocity, the
 1013 APG convection velocity is much lower ($\approx 0.5U_\infty$) than the ZPG one ($\approx 0.8U_\infty$), and its
 1014 value decreases with increasing Clauser parameter. Both trends on coherence lengths and
 1015 convection velocity with APG can in turn be related to a change in the TBL structure as the
 1016 flow moves downstream next to the TE, with larger lifted hairpin-type vortices developing
 1017 away from the wall. When scaled with the friction velocity u_τ ([inner variables](#)), the convection
 1018 velocity, the third key parameter to trailing-edge noise predictions, is seen to collapse over
 1019 a large range of frequencies or streamwise wavenumbers for all four positions (both ZPG
 1020 and APG). [This is consistent with the observed scaling of the streamwise correlation length.](#)
 1021 [This study details non-equilibrium APG effects on a boundary layer and provides significant](#)
 1022 [implications for trailing-edge noise modelling.](#)

1023 Acknowledgments

1024 The research work of A. Caiazzo has been supported by Mitacs through the Mitacs Accelerate
 1025 project IT16104 in collaboration with Mecanum Inc. The authors gratefully acknowledge Dr
 1026 P. Jaiswal for the experimental data.

1027 **Declaration of interests.** The authors report no conflict of interest.

REFERENCES

- 1028 ABE, H. 2017 Reynolds-number dependence of wall-pressure fluctuations in a pressure-induced turbulent
1029 separation bubble. *J. Fluid Mech.* **833**, 563–598, <https://doi.org/10.1017/jfm.2017.694>.
- 1030 ABE, H., MATSUO, Y. & KAWAMURA, H. 2005 A DNS study of Reynolds-number dependence on pressure
1031 fluctuations in a turbulent channel flow. *4th International Symposium on Turbulence and Shear Flow
1032 Phenomena* **1**, 189–194.
- 1033 AMIET, R. K. 1976 Noise due to turbulent flow past a trailing edge. *J. Sound Vib.* **47** (3), 387–393.
- 1034 ARGUILLAT, B., RICOT, D., BAILLY, C. & ROBERT, G. 2010 Measured wavenumber: Frequency spectrum
1035 associated with acoustic and aerodynamic wall pressure fluctuations. *J. Acoust. Soc. Am.* **128** (5),
1036 1647–55, <https://doi.org/10.1121/1.3478780>.
- 1037 BLAKE, W. K. 1970 Turbulent boundary-layer wall-pressure fluctuations on smooth and rough walls. *J. Fluid
1038 Mech.* **44**, 637–660, <https://doi.org/10.1017/S0022112070002069>.
- 1039 BLAKE, W. K. 1986 *Mechanics of flow-induced sound and vibration. Vol. I and II*. Academic Press Inc.
- 1040 BOBKE, A., VINUESA, R., ÖRLÜ, R. & SCHLATTER, P. 2017 History effects and near-equilibrium in adverse-
1041 pressure-gradient turbulent boundary layers. *J. Fluid Mech.* **820**, 667–692, [https://doi.org/10.
1042 1017/jfm.2017.236](https://doi.org/10.1017/jfm.2017.236).
- 1043 BRADSHAW, P. 1967 ‘Inactive’ motion and pressure fluctuations in turbulent boundary layers. *J. Fluid Mech.*
1044 **30**, 241–258, <https://doi.org/10.1017/S0022112067001417>.
- 1045 BROOKS, T. F. & HODGSON, T. H. 1981 Trailing edge noise prediction from measured surface pressures. *J.
1046 Sound Vib.* **78** (1), 69–117, [https://doi.org/10.1016/S0022-460X\(81\)80158-7](https://doi.org/10.1016/S0022-460X(81)80158-7).
- 1047 BULL, M. K. 1967 Wall-pressure fluctuations associated with subsonic turbulent boundary layer flow. *J.
1048 Fluid Mech.* **28**, 719 – 754, <https://doi.org/10.1017/S0022112067002411>.
- 1049 BULL, M. K. 1996 Wall-pressure fluctuations beneath turbulent boundary layers: Some reflections on forty
1050 years of research. *J. Sound Vib.* **190**, 299–315, <https://doi.org/10.1006/jsvi.1996.0066>.
- 1051 BURTON, T. E. 1973 Wall pressure fluctuations at smooth and rough surfaces under turbulent boundary layers
1052 with favorable and adverse pressure gradients. *Tech. Rep.*. Report ONR AD Massachusetts, Institute
1053 of Technology.
- 1054 CAIAZZO, A., ALUJEVIĆ, N., PLUYMERS, B. & DESMET, W. 2018 Active control of turbulent boundary layer-
1055 induced sound transmission through the cavity-backed double panels. *J. Sound Vib.* **422**, 161–188,
1056 <https://doi.org/10.1016/j.jsv.2018.02.027>.
- 1057 CAIAZZO, A., D’AMICO, R. & DESMET, W. 2016 A generalized corcos model for modelling turbulent boundary
1058 layer wall pressure fluctuations. *J. Sound Vib.* **372**, 192–210, [https://doi.org/10.1016/j.jsv.
1059 2016.02.036](https://doi.org/10.1016/j.jsv.2016.02.036).
- 1060 CARPENTER, M. H., NORDSTRÖM, J. & GOTTLIEB, D. 1999 A stable and conservative interface treatment of
1061 arbitrary spatial accuracy. *J. Comp. Phys.* **148**, 341–365.
- 1062 CHOI, H. & MOIN, P. 1990 On the space-time characteristics of wall-pressure fluctuations. *Phys. Fluids A* **2**,
1063 1450–1460, <https://doi.org/10.1063/1.857593>.
- 1064 CHRISTOPHE, J., MOREAU, S., HAMMAN, C. W., WITTEVEEN, J. A. S. & IACCARINO, G. 2015 Uncertainty
1065 Quantification for the Trailing-Edge Noise of a Controlled-Diffusion Airfoil. *AIAA J.* **53** (1), 42–54.
- 1066 CIAPPI, E., DE ROSA, S., FRANCO, F., GUYADER, J.-L., HAMBRIC, S. A., LEUNG, R. C. K. & HANFORD, A. D.
1067 2019 *Flinovia—Flow Induced Noise and Vibration Issues and Aspects-II: A Focus on Measurement,
1068 Modeling, Simulation and Reproduction of the Flow Excitation and Flow Induced Response*. Springer
1069 Nature Switzerland AG, [10.1007/978-3-319-76780-2](https://doi.org/10.1007/978-3-319-76780-2).
- 1070 CIPOLLA, K. & KEITH, W. 2000 Effects of pressure gradients on turbulent boundary layer wave number
1071 frequency spectra. *AIAA J.* **38**, 1832–1836, <https://doi.org/10.2514/2.864>.
- 1072 COHEN, E. & GLOERFELT, X. 2018 Influence of pressure gradients on wall pressure beneath a turbulent
1073 boundary layer. *J. Fluid Mech.* **838**, 715–758, <https://doi.org/10.1017/jfm.2017.898>.
- 1074 COMTE-BELLOT, G. & CORRISIN, S. 1971 Simple eulerian time correlation of full and narrow-band velocity
1075 signals in grid-generated isotropic turbulence. *J. Fluid Mech.* **48**, 273–337, [https://doi.org/10.
1076 1017/S0022112071001599](https://doi.org/10.1017/S0022112071001599).
- 1077 CORCOS, G. M. 1962 *Pressure fluctuations in shear flows. IER reports* 183. Univ. Calif. Inst. Eng. Res.
- 1078 CORCOS, G. M. 1964 The structure of the turbulent pressure field in boundary-layer flows. *J. Fluid Mech.*
1079 **18**, 353–378.

- 1080 CURLE, N. 1955 The influence of solid boundaries upon aerodynamic sound. *Proc. Math. Phys. Eng. Sci.*
1081 **A231**, 505–514, <https://doi.org/10.1098/rspa.1955.0191>.
- 1082 DEL ÁLAMO, J. C. & JIMÉNEZ, J. 2009 Estimation of turbulent convection velocities and corrections to
1083 Taylor’s approximation. *J. Fluid Mech.* **640**, 5–26.
- 1084 DOMINIQUE, J., VAN DEN BERGHE, J., SCHRAM, C. & MENDEZ, M. A. 2022 Artificial neural networks
1085 modeling of wall pressure spectra beneath turbulent boundary layers. *Phys. Fluids* **34** (3), 035119:
1086 1–19.
- 1087 ECKELMANN, H. 1988 A review of knowledge on pressure fluctuations. In *Near-Wall Turbulence: 1988 Zoran*
1088 *Zaric Memorial Conference*, pp. 328–347. Hemisphere, NY.
- 1089 FARABEE, T. M. & CASARELLA, M. J. 1991 Spectral features of wall pressure fluctuations beneath turbulent
1090 boundary layers. *Phys. Fluids A*, **3**, 2410–2420, <https://doi.org/10.1063/1.858179>.
- 1091 FFWOWCS-WILLIAMS, J. E. & HALL, L. H. 1970 Aerodynamic sound generation by turbulent flow in the vicinity
1092 of a scattering half-plane. *J. Fluid Mech.* **40**, 657–670.
- 1093 GOLDSCHMIDT, V. W., YOUNG, M. F. & OTT, E. S. 1981 Turbulent convective velocities (broadband and
1094 wavenumber dependent) in a plane jet. *J. Fluid Mech.* **105**, 327–345.
- 1095 GOODY, M. 2004 Empirical spectral model of surface pressure fluctuations. *AIAA J.* **42** (9), 1788–1794,
1096 <https://doi.org/10.2514/1.9433>.
- 1097 GRAHAM, W. R. 1996 Boundary layer induced noise in aircraft, part I: The flat plate model. *J. Sound Vib.*
1098 **192** (1), 101–120, <https://doi.org/10.1006/jsvi.1996.0178>.
- 1099 GRAHAM, W. R. 1997 A comparison of models for the wavenumber–frequency spectrum of turbulent
1100 boundary layer pressures. *J. Sound Vib.* **206**, 541–565, [https://doi.org/10.1006/jsvi.1997.](https://doi.org/10.1006/jsvi.1997.1114)
1101 **1114**.
- 1102 GRASSO, G., JAISWAL, P., WU, H., MOREAU, S. & ROGER, M. 2019 Analytical models of the wall-pressure
1103 spectrum under a turbulent boundary layer with adverse pressure gradient. *J. Fluid Mech.* **877**,
1104 1007–1062, <https://doi.org/10.1017/jfm.2019.616>.
- 1105 GRAVANTE, S. P., NAGUIB, A. M., WARK, C. E. & NAGIB, H. M. 1998 Characterization of the pressure
1106 fluctuations under a fully developed turbulent boundary layer. *AIAA J.* **36** (10), 1808–1816.
- 1107 GRIFFIN, K. P., FU, L. & MOIN, P. 2021 General method for determining the boundary layer thickness
1108 in nonequilibrium flows. *Phys. Rev. Fluids* **6**, 024608:1–22, [https://doi.org/10.1103/](https://doi.org/10.1103/PhysRevFluids.6.024608)
1109 [PhysRevFluids.6.024608](https://doi.org/10.1103/PhysRevFluids.6.024608).
- 1110 HOWE, M. S. 1978 A review of the theory of trailing edge noise. *J. Sound Vib.* **61** (3), 437–465.
- 1111 HU, N. 2021 Coherence of wall pressure fluctuations in zero and adverse pressure gradients. *J. Sound Vib.*
1112 **511**, 116316, <https://doi.org/10.1016/j.jsv.2021.116316>.
- 1113 HUSSAIN, A. K. M. F. & CLARK, A. R. 1981 Measurements of wavenumber-celerity spectrum in plane and
1114 axisymmetric jets. *AIAA J.* **19** (1), 51–55.
- 1115 HWANG, Y. F., BONNESS, W. K. & HAMBRIC, S. A. 2009 Comparison of semi-empirical models for turbulent
1116 boundary layer wall pressure spectra. *J. Sound Vib.* **319** (1-2), 199–217.
- 1117 JAISWAL, PRATEEK 2020 Experimental investigation of airfoil self-noise. PhD thesis, Université de
1118 Sherbrooke.
- 1119 JAISWAL, P., MOREAU, S., AVALLONE, F., RAGNI, D. & S., PRÖBSTING 2020 On the use of two-point velocity
1120 correlation in wall-pressure models for turbulent flow past a trailing edge under adverse pressure
1121 gradient. *Phys. Fluids* **32** (10), 105105: 1–27, <https://doi.org/10.1063/5.0021121>.
- 1122 JONES, L. E., SANDBERG, R. D. & SANDHAM, N. D. 2008 Direct numerical simulations of forced and unforced
1123 separation bubbles on an airfoil at incidence. *J. Fluid Mech.* **602**, 175–207.
- 1124 KEITH, W. L., HURDIS, D. A. & ABRAHAM, B. M. 1992 A comparison of turbulent boundary layer wall-
1125 pressure spectra. *J. Fluids Eng.* **114**, 338–347.
- 1126 KENNEDY, C. A., CARPENTER, M. H. & LEWIS, R. M. 1999 Low-storage, explicit Runge-Kutta schemes for
1127 the compressible Navier-Stokes equations. *Applied Numerical Mathematics* **35**, 177–219.
- 1128 KIM, J. 1989 On the structure of pressure fluctuations in simulated turbulent channel flow. *J. Fluid Mech.*
1129 **205**, 421–451.
- 1130 KITSIOS, V., ATKINSON, C., SILLERO, J. A., BORRELL, G., GUNGOR, A. G., JIMÉNEZ, J. & SORIA, J. 2016 Direct
1131 numerical simulation of a self-similar adverse pressure gradient turbulent boundary layer. *Int. J. Heat*
1132 *Fluid Fl.* **61**, 129–136, <https://doi.org/10.1016/j.ijheatfluidflow.2016.04.008>.
- 1133 LEE, J.-H. & SUNG, H. J. 2008 Effects of an adverse pressure gradient on a turbulent boundary layer. *Int. J.*
1134 *Heat Fluid Fl.* **29** (3), 568–578.
- 1135 LEE, S., AYTON, L., BERTAGNOLIO, F., MOREAU, S., CHONG, T. P. & JOSEPH, P. 2021 Turbulent boundary

- 1136 layer trailing-edge noise: Theory, computation, experiment, and application. *Prog. Aerosp. Sci.* **126**,
 1137 100737: 1–56, <https://doi.org/10.1016/j.paerosci.2021.100737>.
- 1138 MACIEL, Y., ROSSIGNOL, K.-S. & LEMAY, J. 2006 Self-similarity in the outer region of adverse-pressure-
 1139 gradient turbulent boundary layers. *AIAA J.* **44** (11), 2450–2464, [https://doi.org/10.2514/1.](https://doi.org/10.2514/1.19234)
 1140 [19234](https://doi.org/10.2514/1.19234).
- 1141 MELLOR, G. L. & GIBSON, D. M. 1966 Equilibrium turbulent boundary layers. *J. Fluid Mech.* **24** (2),
 1142 225–253.
- 1143 MESSITER, AF 1970 Boundary-layer flow near the trailing edge of a flat plate. *SIAM Journal on Applied*
 1144 *Mathematics* **18** (1), 241–257.
- 1145 MOIN, P. 2009 Revisiting Taylor’s hypothesis. *J. Fluid Mech.* **640**, 1–4.
- 1146 MONKEWITZ, P. A., CHAUHAN, K. A. & NAGIB, H. M. 2007 Self-consistent high-Reynolds-number
 1147 asymptotics for zero-pressure-gradient turbulent boundary layers. *Phys. Fluids* **19** (11), 115101.
- 1148 MONTY, J. P., HARUN, Z. & MARUSIC, I. 2011 A parametric study of adverse pressure gradient
 1149 turbulent boundary layers. *Int. J. Heat Fluid Fl.* **32** (3), 575–585, [https://doi.org/10.1016/j.](https://doi.org/10.1016/j.ijheatfluidflow.2011.03.004)
 1150 [ijheatfluidflow.2011.03.004](https://doi.org/10.1016/j.ijheatfluidflow.2011.03.004).
- 1151 MOREAU, S. 2016 CD-day. In *Symposium on the CD airfoil*. Lyon, France, [https://www.researchgate.](https://www.researchgate.net/publication/304582435_CD-day_S-Moreau)
 1152 [net/publication/304582435_CD-day_S-Moreau](https://www.researchgate.net/publication/304582435_CD-day_S-Moreau).
- 1153 MOREAU, S., HENNER, M., IACCARINO, G., WANG, M. & ROGER, M. 2003 Analysis of flow conditions in
 1154 freejet experiments for studying airfoil self-noise. *AIAA J.* **41** (10), 1895–1905.
- 1155 MOREAU, S. & ROGER, M. 2005 Effect of airfoil aerodynamic loading on trailing edge noise sources. *AIAA*
 1156 *J.* **43** (1), 41–52.
- 1157 MOREAU, S. & ROGER, M. 2009 Back-scattering correction and further extensions of Amiet’s trailing-edge
 1158 noise model. Part II: Application. *J. Sound Vib.* **323** (1-2), 397–425, [https://doi.org/10.1016/](https://doi.org/10.1016/j.jsv.2008.11.051)
 1159 [j.jsv.2008.11.051](https://doi.org/10.1016/j.jsv.2008.11.051).
- 1160 MOREAU, S., SANJOSÉ, M., PÉROT, F. & KIM, M.-S. 2011 Direct self-noise simulation of the installed
 1161 controlled diffusion airfoil. In *17th AIAA/CEAS Aeroacoustics Conference*. Portland, OR: AIAA,
 1162 <https://doi.org/10.2514/6.2011-2716>.
- 1163 NA, Y. & MOIN, P. 1998 The structure of wall-pressure fluctuations in turbulent boundary layers with adverse
 1164 pressure gradient and separation. *J. Fluid Mech.* **377** (3), 347–373.
- 1165 NAGIB, H. M. & CHAUHAN, K. A. 2008 Variations of von Kármán coefficient in canonical flows. *Phys.*
 1166 *Fluids* **20** (10), 101518, <https://doi.org/10.1063/1.3006423>.
- 1167 NEAL, D. R. 2010 The effects of rotation on the flow field over a controlled-diffusion airfoil. PhD thesis,
 1168 Michigan State University.
- 1169 NICKELS, T. B. 2004 Inner scaling for wall-bounded flows subject to large pressure gradients. *J. Fluid Mech.*
 1170 **521**, 217–239, <https://doi.org/10.1017/S0022112004001788>.
- 1171 PADOIS, T., LAFFAY, P., IDIER, A. & MOREAU, S. 2015 Detailed experimental investigation of the aeroacoustic
 1172 field around a controlled-diffusion airfoil. In *21st AIAA/CEAS Aeroacoustics Conference*. Dallas,
 1173 TX: American Institute of Aeronautics and Astronautics.
- 1174 PALUMBO, D. 2012 Determining correlation and coherence lengths in turbulent boundary layer flight data.
 1175 *J. Sound Vib.* **331** (16), 3721–3737.
- 1176 PANTON, R. L. & LINEBARGER, J. H. 1974 Wall pressure spectra calculations for equilibrium boundary layers.
 1177 *J. Fluid Mech.* **65** (2), 261–287, <https://doi.org/10.1017/S0022112074001388>.
- 1178 PARGAL, S., WU, H., YUAN, J. & MOREAU, S. 2022 Adverse-pressure-gradient turbulent boundary layer on
 1179 convex wall. *Phys. Fluids* **34** (3), 035107:1–13.
- 1180 ROGER, M. & MOREAU, S. 2005 Back-scattering correction and further extensions of Amiet’s trailing edge
 1181 noise model. Part I: theory. *J. Sound Vib.* **286** (3), 477–506, [https://doi.org/10.1016/j.](https://doi.org/10.1016/j.jsv.2004.10.054)
 1182 [jsv.2004.10.054](https://doi.org/10.1016/j.jsv.2004.10.054).
- 1183 ROGER, M. & MOREAU, S. 2012 Addendum to the back-scattering correction of Amiet’s trailing-edge noise
 1184 model. *J. Sound Vib.* **331** (24), 5383–5385, <https://doi.org/10.1016/j.jsv.2012.06.019>.
- 1185 ROZENBERG, Y., ROBERT, G. & MOREAU, S. 2012 Wall-pressure spectral model including the adverse pressure
 1186 gradient effects. *AIAA J.* **50** (10), 2168–2179, <https://doi.org/10.2514/1.J051500>.
- 1187 SALZE, E., BAILLY, C., MARSDEN, O., JONDEAU, E. & JUVÉ, D. 2014 An experimental characterisation of wall
 1188 pressure wavevector-frequency spectra in the presence of pressure gradients. In *20th AIAA/CEAS*
 1189 *Aeroacoustics Conference*. Atlanta, GA: American Institute of Aeronautics and Astronautics.
- 1190 SALZE, E., BAILLY, C., MARSDEN, O., JONDEAU, E. & JUVÉ, D. 2015 An experimental investigation of wall
 1191 pressure fluctuations beneath pressure gradients. In *21th AIAA/CEAS Aeroacoustics Conference*.
 1192 Dallas, TX: American Institute of Aeronautics and Astronautics.

- 1193 SANDBERG, R. D. 2015 Compressible-flow DNS with application to airfoil noise. *Flow, Turb. Comb.* **95**,
1194 211–229.
- 1195 SANDBERG, R. D. & SANDHAM, N. D. 2006 Nonreflecting zonal characteristic boundary condition for direct
1196 numerical simulation of aerodynamic sound. *AIAA J.* **44**, 402–405.
- 1197 SANJOSÉ, M. & MOREAU, S. 2018 Fast and accurate analytical modeling of broadband noise for a low-speed
1198 fan. *J. Acoust. Soc. Am.* **143** (5), 3103–3113, <https://doi.org/10.1121/1.5038265>.
- 1199 SCHEWE, G. 1983 On the structure and resolution of wall-pressure fluctuations associated with turbulent
1200 boundary-layer flow. *J. Fluid Mech.* **134**, 311–328.
- 1201 SCHLATTER, P., LI, Q., BRETHOUWER, G., JOHANSSON, A. V. & HENNINGSON, D. S. 2009a High-Reynolds
1202 number turbulent boundary layers studied by numerical simulation. *Bull. Am. Phys. Soc.* **54**.
- 1203 SCHLATTER, P. & ÖRLÜ, R. 2010 Assessment of direct numerical simulation data of turbulent boundary
1204 layers. *J. Fluid Mech.* **659**, 116–126, <https://doi.org/10.1017/S0022112010003113>.
- 1205 SCHLATTER, P., ÖRLÜ, R., LI, Q., BRETHOUWER, G., FRANSSON, J. H. M., JOHANSSON, A. V., ALFREDSSON,
1206 P. H. & HENNINGSON, D. S. 2009b Turbulent boundary layers up to $Re_{\theta} = 2500$ studied through
1207 simulation and experiment. *Phys. Fluids* **21** (5), 051702.
- 1208 SCHLICHTING, H. & GERSTEN, K. 2017 *Boundary-layer theory*. Springer.
- 1209 SCHLOEMER, H. H. 1967 Effects of pressure gradients on turbulent-boundary-layer wall-pressure fluctuations.
1210 *J. Acoust. Soc. Am.* **42** (1), 93–113.
- 1211 SILLERO, J. A., JIMÉNEZ, J. & MOSER, R. D. 2014 Two-point statistics for turbulent boundary layers and
1212 channels at reynolds numbers up to $\delta^+ \approx 2000$. *Phys. Fluids* **26** (10), 105109:1–31.
- 1213 SIMPSON, R. L., GHODBANE, M. & McGRATH, B. E. 1987 Surface pressure fluctuations in a separating
1214 turbulent boundary layer. *Journal of Fluid Mechanics* **177**, 167–186.
- 1215 SKOTE, M., HENNINGSON, D. S. & HENKES, R. A. W. M. 1998 Direct numerical simulation of self-similar
1216 turbulent boundary layers in adverse pressure gradients. *Flow Turb. Comb.* **60** (1), 47–85.
- 1217 SMITS, A. J., MATHESON, N. & JOUBERT, P. N. 1983 Low-Reynolds-number turbulent boundary layers in
1218 zero and favorable pressure gradients. *J. Ship Res.* **27** (03), 147–157.
- 1219 SPALART, P. R. 1988 Direct simulation of a turbulent boundary layer up to $Re_{\theta} = 1410$. *J. Fluid Mech.* **187**,
1220 61–98.
- 1221 TAM, C. K. W. & YU, J. C. 1975 Trailing edge noise. In *2nd Aeroacoustics Conference*. American Institute
1222 of Aeronautics and Astronautics, <https://doi.org/10.2514/6.1975-489>.
- 1223 TANARRO, Á., VINUESA, R. & SCHLATTER, P. 2020 Effect of adverse pressure gradients on turbulent wing
1224 boundary layers. *J. Fluid Mech.* **883** (A8), <https://doi.org/10.1017/jfm.2019.838>.
- 1225 TAYLOR, G. I. 1938 The spectrum of turbulence. *Proc. R. Soc. A: Math. Phys. Eng. Sci.* **164** (919), 476 –
1226 490.
- 1227 TOWNSEND, A. A. 1961 Equilibrium layers and wall turbulence. *J. Fluid Mech.* **11** (1), 97–120.
- 1228 VAN BLITTERSWYK, J. & ROCHA, J. 2017 An experimental study of the wall-pressure fluctuations beneath
1229 low Reynolds number turbulent boundary layers. *J. Acoust. Soc. Am.* **141** (2), 1257–1268, <https://doi.org/10.1121/1.4976341>.
- 1230
1231 VILA, C. S., ÖRLÜ, R., VINUESA, R., SCHLATTER, P., IANIRO, A. & DISCETTI, S. 2017 Adverse-pressure-
1232 gradient effects on turbulent boundary layers: statistics and flow-field organization. *Flow Turb.*
1233 *Comb.* **99** (3), 589–612.
- 1234 VINUESA, R., HOSSEINI, S. M., HANIFI, A., HENNINGSON, D. S. & SCHLATTER, P. 2017 Pressure-gradient
1235 turbulent boundary layers developing around a wing section. *Flow Turb. Comb.* **99** (3), 613–641,
1236 <https://doi.org/10.1007/s10494-017-9840-z>.
- 1237 VOLINO, R. J. 2020 Non-equilibrium development in turbulent boundary layers with changing pressure
1238 gradients. *J. Fluid Mech.* **897** (A2), <https://doi.org/10.1017/jfm.2020.319>.
- 1239 VON KÁRMÁN, T. H. 1931 *NACA Technical memorandum 611*. National Advisory Committee for Aeronautics.
- 1240 WANG, M., MOREAU, S., IACCARINO, G. & ROGER, M. 2009 LES prediction of wall-pressure fluctuations and
1241 noise of a low-speed airfoil. *Int. J. Aeroacoust.* **8** (3), 177–197.
- 1242 WATMUFF, J. H. 1989 An experimental investigation of a low Reynolds number turbulent boundary layer
1243 subject to an adverse pressure gradient. *Ann. Res. Briefs* pp. 37–49.
- 1244 WILLMARTH, W. W. 1956 Wall pressure fluctuations in a turbulent boundary layer. *J. Acoust. Soc. Am.* **28** (6),
1245 1048–1053.
- 1246 WILLMARTH, W. W. 1975 Pressure fluctuations beneath turbulent boundary layers. *Ann. Rev. Fluid Mech.*
1247 **7** (1), 13–36.
- 1248 WILLS, J. A. B. 1964 On convection velocities in turbulent shear flows. *J. Fluid Mech.* **20**, 417–432.
- 1249 WU, H., MOREAU, S. & SANDBERG, R. D. 2019 Effects of pressure gradient on the evolution of velocity-

- 1250 gradient tensor invariant dynamics on a controlled-diffusion aerofoil at $Re_c = 150000$. *J. Fluid*
1251 *Mech.* **868**, 584–610, <https://doi.org/10.1017/jfm.2019.129>.
- 1252 WU, H., MOREAU, S. & SANDBERG, R. D. 2020 On the noise generated by a controlled-diffusion aerofoil at
1253 $Re_c = 1.5 \times 10^5$. *J. Sound Vib.* **487**, 115620, <https://doi.org/10.1016/j.jsv.2020.115620>.
- 1254 WU, H., SANJOSE, M., MOREAU, S. & SANDBERG, R. D. 2018 Direct numerical simulation of the self-
1255 noise radiated by the installed controlled-diffusion airfoil at transitional reynolds number. In
1256 *24th AIAA/CEAS Aeroacoustics Conference*. Atlanta, GA: American Institute of Aeronautics and
1257 Astronautics, <https://doi.org/10.2514/6.2018-3797>.
- 1258 WU, X., MOIN, P., WALLACE, J. M., SKARDA, J. A., LOZANO-DURÁN & HICKEY, J.-P. 2017 Transitional-
1259 turbulent spots and turbulent-turbulent spots in boundary layers. *Proc. Natl Acad.* **114**, E5292 –
1260 E5299, <https://doi.org/10.1073/pnas.1704671114>.
- 1261 ZHOU, J., ADRIAN, R. J., BALACHANDAR, S. & KENDALL, T. M. 1999 Mechanisms for generating coherent
1262 packets of hairpin vortices in channel flow. *J. Fluid Mech.* **387**, 353–396, [https://doi.org/10.](https://doi.org/10.1017/S002211209900467X)
1263 [1017/S002211209900467X](https://doi.org/10.1017/S002211209900467X).